Biomaterials 306 (2024) 122473

Contents lists available at ScienceDirect

Biomaterials

journal homepage: www.elsevier.com/locate/biomaterials

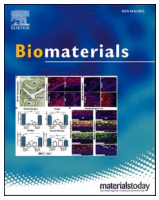

Stiffness assisted cell-matrix remodeling trigger 3D mechanotransduction regulatory programs

Anna L. Kersey [a], Daniel Y. Cheng [a], Kaivalya A. Deo [a], Christina R. Dubell [a], Ting-Ching Wang [a], Manish K. Jaiswal [a], Min Hee Kim [a], Aparna Murali [a], Sarah E. Hargett [a], Sumana Mallick [a,b], Tanmay P. Lele [a], Irtisha Singh [a,b,c,**], Akhilesh K. Gaharwar [a,c,d,e,*]

[a] Department of Biomedical Engineering, College of Engineering, Texas A&M University, College Station, TX 77843, USA
[b] Department of Cell Biology and Genetics, School of Medicine, Texas A&M University, Bryan, TX 77807, USA
[c] Interdisciplinary Program in Genetics, Texas A&M University, College Station, TX 77843, USA
[d] Center for Remote Health Technologies and Systems, Texas A&M University, College Station, TX 77843, USA
[e] Department of Material Science and Engineering, College of Engineering, Texas A&M University, College Station, TX 77843, USA

ARTICLE INFO

Keywords:
Biomaterials
Regenerative medicine
Three-dimensional (3D) microenvironment
Disease modelling
Mechanotransduction

ABSTRACT

Engineered matrices provide a valuable platform to understand the impact of biophysical factors on cellular behavior such as migration, proliferation, differentiation, and tissue remodeling, through mechanotransduction. While recent studies have identified some mechanisms of 3D mechanotransduction, there is still a critical knowledge gap in comprehending the interplay between 3D confinement, ECM properties, and cellular behavior. Specifically, the role of matrix stiffness in directing cellular fate in 3D microenvironment, independent of viscoelasticity, microstructure, and ligand density remains poorly understood. To address this gap, we designed a nanoparticle crosslinker to reinforce collagen-based hydrogels without altering their chemical composition, microstructure, viscoelasticity, and density of cell-adhesion ligand and utilized it to understand cellular dynamics. This crosslinking mechanism utilizes nanoparticles as crosslink epicenter, resulting in 10-fold increase in mechanical stiffness, without other changes. Human mesenchymal stem cells (hMSCs) encapsulated in 3D responded to mechanical stiffness by displaying circular morphology on soft hydrogels (5 kPa) and elongated morphology on stiff hydrogels (30 kPa). Stiff hydrogels facilitated the production and remodeling of nascent extracellular matrix (ECM) and activated mechanotransduction cascade. These changes were driven through intracellular PI3AKT signaling, regulation of epigenetic modifiers and activation of YAP/TAZ signaling. Overall, our study introduces a unique biomaterials platform to understand cell–ECM mechanotransduction in 3D for regenerative medicine as well as disease modelling.

1. Introduction

Extracellular matrices (ECMs) provide physical support and biochemical signaling cues for cells. Their mechanical properties play a critical role in regulating a wide range of cellular behaviors, including differentiation, migration, and proliferation [1–3]. These mechanical properties can include factors such as stiffness, viscoelasticity, and porosity. The process by which cells sense and respond to these mechanical cues is called mechanotransduction. Mechanotransduction involves the conversion of mechanical forces into biochemical signals that drive changes in cell behavior by activation of intracellular signaling pathways, modulation of gene expression, and regulation of cell shape and cytoskeletal organization [4]. This coordination relies on tight regulation of cellular and molecular signaling pathways which are achieved through transcriptomic-epigenetic cross-talk [5,6]. A more comprehensive understanding of the relationship between ECM mechanical properties and mechanotransduction is essential for developing effective therapies for a wide range of diseases, including cancer, cardiovascular disease, and tissue engineering [7,8].

Synthetic hydrogels are often used to study mechanotransduction in 2D microenvironments [9]. Polyacrylamide (PA) hydrogels have been used as a model system to investigate the impact of biophysical cues on

* Corresponding author. Department of Biomedical Engineering, College of Engineering, Texas A&M University, College Station, TX 77843, USA.
** Corresponding author. Department of Cell Biology and Genetics, School of Medicine, Texas A&M University, Bryan, TX 77807, USA.
E-mail addresses: isingh@tamu.edu (I. Singh), gaharwar@tamu.edu (A.K. Gaharwar).

https://doi.org/10.1016/j.biomaterials.2024.122473
Received 11 July 2023; Received in revised form 13 November 2023; Accepted 16 January 2024
Available online 18 January 2024

cellular behavior in 2D microenvironments. By altering the stiffness of PA hydrogels, it is possible to investigate cellular response independent of protein tethering and porosity [10–12]. Polyethylene glycol (PEG) hydrogels allow for the tuning of mechanical stiffness by altering the crosslinking density of the polymer [13,14]. However, the manipulation of crosslinking density can also affect the diffusion of macromolecules, which can complicate the interpretation of studies relying on these hydrogels. Although these synthetic hydrogels are often used to study mechanotransduction in 2D microenvironments, these biomaterials fail to accurately replicate the native 3D microenvironment [9].

Recent studies have emphasized the critical role of 3D confinement in shaping cellular behavior [15–17]. Cells require the ability to exert force in order to spread, migrate, and divide effectively. However, our understanding of 3D cell-ECM mechanotransduction is still evolving, and there is a need for more physiologically relevant 3D models that incorporate genome-wide assays to fully comprehend the mechanistic connections between ECM properties and intracellular signaling [1]. Factors such as matrix restriction-dependent adhesions, volumetric stress fields, and localized cell return forces have been identified to be important in this process. In order to accurately replicate the native ECM microenvironment for studying mechanotransduction in 3D, it is essential to develop 3D engineered matrices that accurately reflect the biophysical and biochemical cues of the ECM. Such models will enable us to gain a comprehensive understanding of the complex interplay between these cues and their regulation of cellular behavior. Moreover, these models will aid in the development of more effective therapies for a wide range of diseases.

To accurately mimic native cell-ECM interactions in 3D, a variety of natural polymers, including purified ECM proteins such as collagen, laminin, and recombinant basement membrane (Matrigel) are used [18–20]. However, increasing the concentration of ECM proteins in hydrogels can increase stiffness, which may confound the interpretation of results since it also increases the density of adhesion ligands available for cellular receptors [21]. Thus, it is crucial to have independent control of the various physical and chemical properties of the synthetic niche. One promising approach to overcome these limitations is the use of alginate hydrogels, which can investigate the effect of mechanical parameters such as viscoelasticity and stiffness independently of ligand density, degradability, and transport on cell-ECM mechanotransduction in 3D [3,13,17,22]. However, the main limitations of these hydrogels is their lack of physiological relevance, as they do not fully replicate the natural ECM of cells in the human body. This may limit the clinical applicability of these hydrogels, as it can be difficult to accurately predict how cells will behave *in vivo*. Therefore, there is still a need to develop 3D models that closely reflect the native ECM microenvironment to improve our understanding of mechanotransduction and its role in disease development and progression.

A promising approach to modulate hydrogel properties notably stiffness, can be achieved through incorporation of nanoparticles [23]. This strategy not only augments the mechanical robustness of the hydrogels but also enables the dynamic alteration of the microenvironment via external stimuli such as magnetic fields, temperature, and photonic energy [24]. A range of nanomaterials have been reported to improve stiffness including graphene [25], carbon nanotubes [26,27], silicates [28], transition metal dichalcogenides [29] and iron oxide [30]. However, a notable limitation of these nanocomposites is the limited increase in matrix stiffness, underscoring the need to explore more efficient alternatives.

To overcome these limitations of synthetic and natural hydrogels, here we propose a unique approach to reinforce collagen-based hydrogels using extremely low concentrations of a nanoparticulate-reinforcing agent that acts as a crosslink epicenter. The addition of these nanoparticles at a 10,000-fold lower concentration relative to polymer resulted in more than 10-fold increase in mechanical stiffness without changing their chemical composition or mesh size, microstructure, viscoelasticity, and density of cell-adhesion ligand. This platform system provides insight on the role of matrix stiffness in directing stem cell differentiation in physiologically relevant 3D microenvironments. In addition, the impact of matrix stiffness on nascent protein adhesion, mechanosensing (YAP/TAZ nuclear translocation and osteogenic differentiation) and chromatin remodeling can be understood in native 3D microenvironment.

2. Results and discussion

2.1. Synthesis and characterization of engineered hydrogels with different stiffness

We have developed a highly efficient method to reinforce polymeric hydrogels using extremely low concentrations (<1000-fold than polymer) of nanoparticle-reinforcing agent than the polymer (see **Methods**). Specifically, we selected nanoparticles (8 nm, Figs. S1A–B) decorated with PEG-dopamine to reinforce gelatin methacrylate (GelMA) by exposing to photopolymerization (Irgacure 2959, 30 mW/cm^2, 60 s) (Fig. 1A). The mechanism of nanoreinforcement has previously been established by our group in which nitro-dopamine functionalized nanoparticle acts as crosslink epicenters [31]. These nanoparticles have the ability to form covalent bonds with multiple amine and carboxylic acid groups present on the GelMA backbone. Specifically, carboxylate-amine association between nanoparticle and prepolymer solutions (GelMA) result in imide bond formation following UV exposure. Thus, mechanical stiffening is achieved due to nanoparticle-driven covalent reinforcement of polymer. The incorporation of nanoparticles at 1000-fold lower concentrations (5 μg/mL) compared to GelMA did not result in any change by gross observation. The highly porous, and interconnected networks of GelMA and nanoreinforced GelMA hydrogels were evaluated using scanning electron microscopy (SEM) (Fig. 1B). No substantial alterations were detected in the microstructure of the lyophilized hydrogels. It is critical to consider that the freeze-drying process employed during SEM sample preparation could potentially introduce artifacts. Nonetheless, our prior investigations [31] corroborate the observed effects of nanoparticles on the porosity and structural integrity of hydrogels.

The impact of nanoparticle addition on hydrogel stiffness was evaluated via uniaxial compression testing (Xpert 7600, ADMET). The compressive stress-strain curve shows a significant increase in mechanical stiffness due to nanoreinforcement (Fig. 1C). A 10-fold increase in compressive modulus was observed due to reinforcement with nanoparticles. The compressive modulus for 5 % GelMA hydrogel was 4.99 ± 0.25 kPa, while the addition of 0.5 μg/mL and 5 μg/mL nanoparticles yielded average compressive moduli of 18.84 ± 7.2 and 39.1 ± 11.6 kPa, respectively. Similarly, addition of nanoparticles resulted in ~3-fold increase in hydrogel toughness compared to GelMA control (Fig. S1C). Average energy dissipation for 5 % GelMA hydrogel was 0.92 ± 0.38 kJ/m^3. Addition of 0.5 μg/mL and 5 μg/mL nanoparticles resulted in 1.66 ± 0.14 and 2.03 ± 0.47 kJ/m^3 average energy dissipation, respectively. This demonstrates that while incorporation of nanoparticles results in slight increase of energy dissipation, the overall change compared to purely GelMA constructs is statistically insignificant (Fig. S1D). Thus, our data suggest that increased compressive stiffness due to nanoreinforcement does not result in significant changes in the elasticity of the hydrogels.

To investigate viscoelasticity of GelMA (soft) and nanoreinforced GelMA (stiff) hydrogels, stress sweep and stress relaxation were performed. A stress sweep was performed to evaluate yield behavior of each hydrogel (Fig. S1E). This demonstrates that stiff hydrogels yield at significantly higher oscillatory stress (17.9 ± 4.58 Pa), further confirming their higher mechanical strength (Fig. S1F). The time sweep experiments indicates that stiff constructs possess a sustained, higher storage and loss moduli than soft gel counterparts at incrementally increasing percent strain Fig. S1G).

The dynamics of stress relaxation were assessed by subjecting

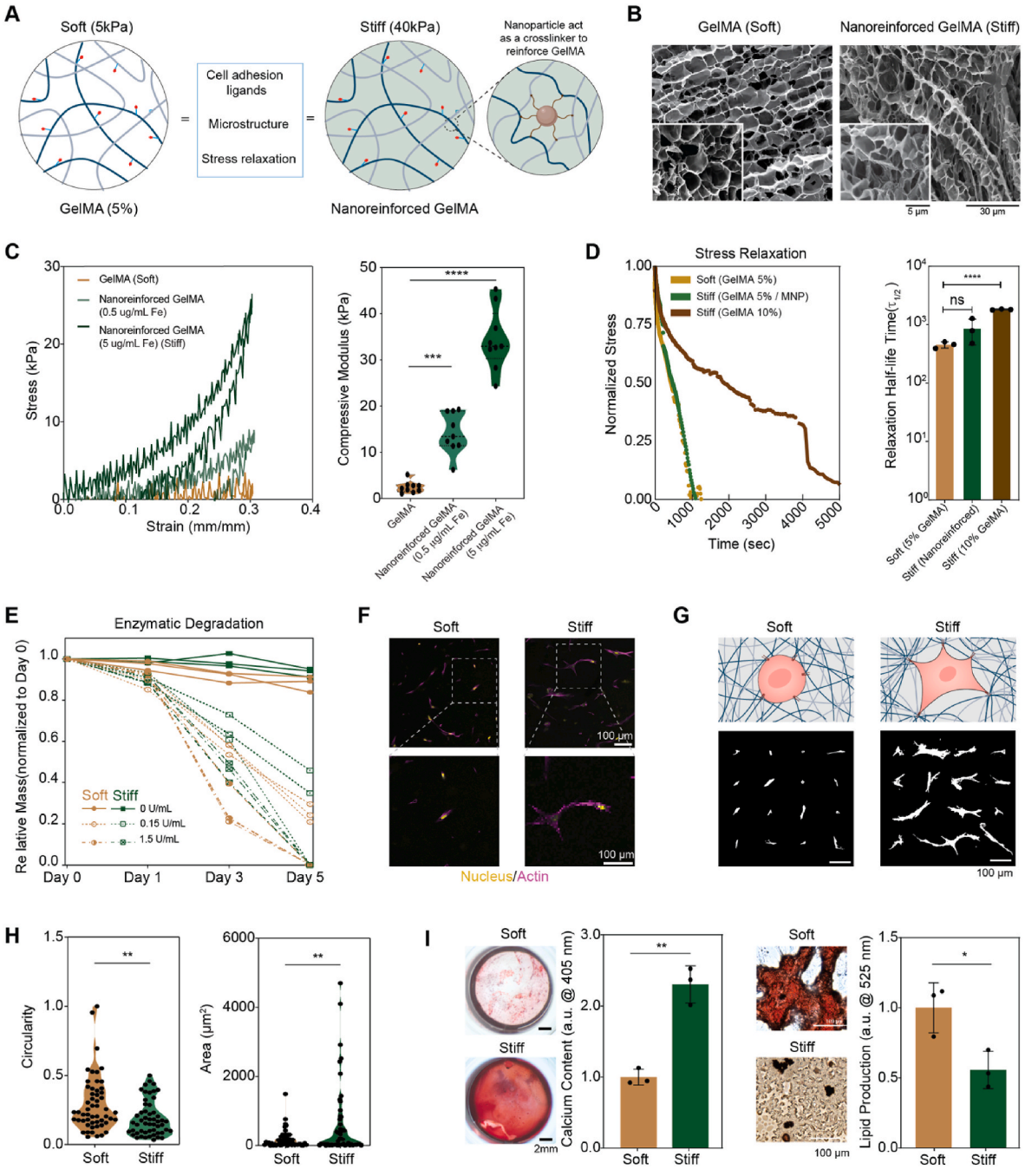

Fig. 1. Mechanical characterization of stiff nanoengineered hydrogels. (A) Schematic illustrating fabrication of soft (GelMA) and stiff hydrogels. Stiff hydrogels are reinforced with nanoparticles with an ability to form covalent crosslinking with multiple GelMA chains. **(B)** Crosslinked hydrogels containing nanoparticles appear visually indistinct from GelMA counterparts. Network porosity visualized via SEM depicted highly interconnected porous structures in both soft and stiff hydrogels. **(C)** Uniaxial compression testing was performed to determine mechanical stiffness of soft and stiff hydrogels. Hydrogels reinforced with varying amounts of nanoparticles (0, 0.5, and 5 μg/mL) result in change in stress-strain curve and compressive stiffness (n = 8, mean ± s.d., $*P \leq 0.05$, one-way ANOVA with Tukey's multiple comparisons). **(D)** Stress relaxation rate of crosslinked hydrogels at 15 % strain reveals insignificant difference in relaxation half-life ($\tau_{1/2}$) between soft (5 % GelMA) and stiff samples (nanoreinforced). 5 % and 10 % GelMA samples possess significantly difference in stress relaxation rates. The bar graph represents the normalized stress relaxation of gels, indicating the time required for each to relax to half of its initial value (n = 3, n.s. $P = 0.3833$, $****P < 0.0001$, one-way ANOVA). **(E)** Degradation profile of soft and stiff hydrogels in presence of different amount of collagenase at 37 °C. The mass of hydrogels is normalized to day 0 mass (n = 3). **(F)** Morphology of cells encapsulated within soft (GelMA) and stiff (nanoreinforced GelMA) hydrogels after day 7. Increased cell spreading is observed in cells encapsulated within stiff hydrogels. Counterstained structures include F-actin (purple) and DAPI (blue). (**G**) Representative single cell images (silhouettes) are arranged in a grid (n = 14–16). Scale bar 100 μm. **(H)** Quantification of circularity and total cell area of hMSCs encapsulated in soft and stiff hydrogels for 7 days by ImageJ analysis of immunostained actin (n > 50, mean ± s.d., $**P < 0.01$, unpaired two tailed *t* tests). **(I)** Differentiation of hMSCs in conditioned media (osteogenic and adipogenic media) after 21 days. The presence of calcium is detected using Alizarin Red S. (ARS) and subset colorimetric quantification (scale bar, 2 mm). The presence of lipid deposition was determined via Oil Red O (scale bar, 100 μm). The bar graph represents absorbance (n = 3, mean ± s.d., $**P \leq 0.01$, $*P \leq 0.05$, unpaired two-tailed *t*-test, one representative image shown). (For interpretation of the references to color in this figure legend, the reader is referred to the Web version of this article.)

hydrogels to a 15 % oscillatory strain. Stress relaxation curves were standardized by scaling the diminishing modulus of each hydrogel against its initial modulus. Analysis demonstrated that hydrogels of lower modulus (453 ± 46 Pa) and those augmented with nanoparticles (847 ± 325 Pa) displayed comparable normalized relaxation half-lives (τ1/2) (Fig. 1D). Conversely, hydrogels with higher GelMA concentration (10 %) presented a markedly elevated stress relaxation rate (1828 ± 27 Pa). These findings suggest that while nanoparticle augmentation enhances the stiffness of hydrogels, their viscoelastic characteristics remain analogous to those of standard GelMA hydrogels. Consequently, this system is optimally configured for investigating cellular responses to variations in matrix stiffness in 3D, devoid of influence from viscoelasticity and ligand density.

Enzymatic degradation of the matrix was quantified to evaluate the effect of reinforcement on crosslink deterioration. Incubation of hydrogels with collagenase for a duration of five days showed that matrices with higher rigidity exhibit a marginally reduced degradation rate compared to their less rigid counterparts (Fig. 1E). Nevertheless, when subjected to elevated levels of an MMP-specific enzyme, both reinforced and non-reinforced hydrogels were fully degraded by the end of five day period. These observations indicate that nanoreinforcement does not impede hydrogel's susceptibility to enzymatic breakdown.

2.2. Matrix stiffness direct cells fate

The physical confinement of cells within a 3D matrix can induce changes in cell shape and cytoskeletal organization, which can in turn modulate intracellular signaling pathways and gene expression [1,5]. To investigate the effect of matrix stiffness on cellular morphology, encapsulated hMSCs were observed after 7 days. Cells encapsulated in soft hydrogels possess a rounded morphology, while cells in stiff hydrogels exhibited elongated morphology (Fig. 1F and G, Supplementary Movie 1 and 2). Microscopic visualization and quantification of the cellular morphology has significant change in cell morphology due to matrix stiffness (Fig. 1H). Quantitative analysis of cell area and circularity further corroborates these findings, indicating that hMSCs encapsulated in rigid hydrogels exhibit an increased cellular footprint, whereas those in pliable hydrogels retain a more rounded phenotype. (Fig. 1H). These findings illustrate that stiff hydrogels (~40 kPa) promote higher degree of cell spreading compared to soft hydrogels (~5 kPa). This has important implications for stem cell differentiation, particularly in the context of osteoblast and adipocyte differentiation [8,32,33].

We hypothesized that hMSCs encapsulated in soft hydrogels (~3 kPa) will undergo adipogenesis, while cells in stiff hydrogels (~30 kPa) will undergo osteogenesis. To confirm this, encapsulated hMSCs were cultured for 21 days in soft and stiff hydrogels. As expected, we detected higher expression of key osteogenic transcription factor, Runt-related transcription factor 2 (RUNX2), in stiff hydrogels (Fig. S1H). Collagen type 1 alpha 1 (COL1A1), an early marker of differentiating pre-osteoblasts, was also upregulated in stiffer microenvironment. After 21 days, 2.3-fold increase in matrix mineralization was observed in stiff hydrogels, as evident by Alizarin Red S. (ARS) staining for calcium deposits (Fig. 1I). Further, osteopontin (OPN) expression was enhanced in stiff hydrogels, as illustrated by immunofluorescent staining (Fig. S1I). In contrast, cells in stiff hydrogels exhibited significantly lower amount (0.55-fold) of lipid production after 21 days as evident by Oil Red O staining (Fig. 1I, Fig. S1J). These data collectively support that stiff hydrogels drive long-term stable phenotypic changes in hMSCs. This aligns with previous reports demonstrating that mechanical signals are transmitted to cells to regulate transcription factors such as RUNX2 and PPAR-γ, which play a pivotal role in driving commitment towards osteogenic or adipogenic lineages, respectively [9,10,34–36].

2.3. Matrix stiffness influence transcriptomic landscape

We evaluated the cellular response of hMSCs encapsulated in soft and stiff hydrogels by conducting whole transcriptome sequencing (RNA-seq) at Day 7. To capture the transcriptomic changes that occur in the early stages of differentiation, we extracted RNA on Day 7 for performing RNA-seq. We first encapsulated hMSCs into soft and stiff hydrogels, as previously described (see **Methods**). After 7 days, we extracted mRNA from the hydrogels using Trizol reagent and then sequenced the mRNA on the DNBseq platform. The sequenced reads were aligned to the human genome (hg38) using STAR aligner [37]. Principal component analysis (PCA) was performed to assess variability within sample groups. This showed that the PC1 that captured majority of variance (PC1, 58.59 %) separated the two experimental groups (soft and stiff), with limited variation (PC2, 16.03 %) between technical replicates within each group (Fig. 2A). We quantified the expression of each gene in fragments per kilobase million (FPKM) and with our criteria detected 9678 genes that are expressed robustly across samples (see Methods and Supplementary Table 1). Gene expression profile of cells obtained from stiff hydrogel sample conditions were compared to soft hydrogel group. Generalized linear models (GLMs) were used to identify differentially expressed genes (DEGs) between the two conditions [38] (see Methods). We detected 1,751 DEGs (*Padj.* < 0.05). Stiff hydrogels promoted significantly higher expression of 948 genes and resulted in downregulation of 803 genes (*Padj.* < 0.05) (Fig. 2B). Hierarchical clustering of all DEGs confirmed that the replicates of each condition have similar expression levels for these genes, and that the soft and stiff groups had distinct gene expression profiles (Fig. 2C).

To understand the significant biological processes (BP) associated with DEGs, we conducted a Gene Ontology (GO) overrepresentation analysis. Using a conservative statistical cutoff of $P < 0.01$, we identified 411 significantly enriched GO terms. These terms were then grouped into categories, such as adhesion, motility, signaling, transcription, and osteogenic differentiation (Fig. 2D and Supplementary Table 2). This analysis suggested perturbation of BP involving interactions between ECM receptors and cell surface proteins, activation of small GTPase molecules and focal adhesion complex assembly. Further analysis of GO Molecular Functions (MF) and Cellular Component (CC) ontologies confirmed that extracellular matrix structural components, GTPase activators, transmembrane protein kinases, and focal adhesion complexes are differentially affected between stiff and soft hydrogel culture (Figs. S2A–B).

2.4. Matrix stiffness promotes expression of mechanically-sensitive genes and proteins

The ECM provides mechanical signals that cells can respond to through the activation of mechanosensitive transmembrane molecules, which anchor the cells to the surrounding matrix [39]. The mechanical signals also trigger the expression of cell surface peptides that signal the sequestration of nascent proteins at the cell-ECM interface, and the initiation of matrix remodeling enzymes that degrade existing ECM and allow cells to deposit new ECM [2]. We observed that cells seeded in softer matrix (~5 kPa) exhibit limited cell-matrix adhesion and activation of cytoskeletal projections that is required for cell motility and spreading. In contrast, stiff hydrogels (~40 kPa) provide adequate cell-matrix interactions by activating cell surface proteins (Fig. S3A). This process includes activation of mechanosensitive transmembrane molecules to anchor cells to the surrounding matrix, expression of cell surface peptides that signal the sequestration of nascent proteins at the cell-ECM interface, and, finally, initiation of matrix remodeling enzymes to strategically degrade existing ECM and allow cells to deposit nascent ECM (Fig. 3A).

To gain a deeper understanding of the signal transduction activated by stiff hydrogels, genes in highly enriched GO terms were analyzed. The three most significant GO terms that were identified by GO BP

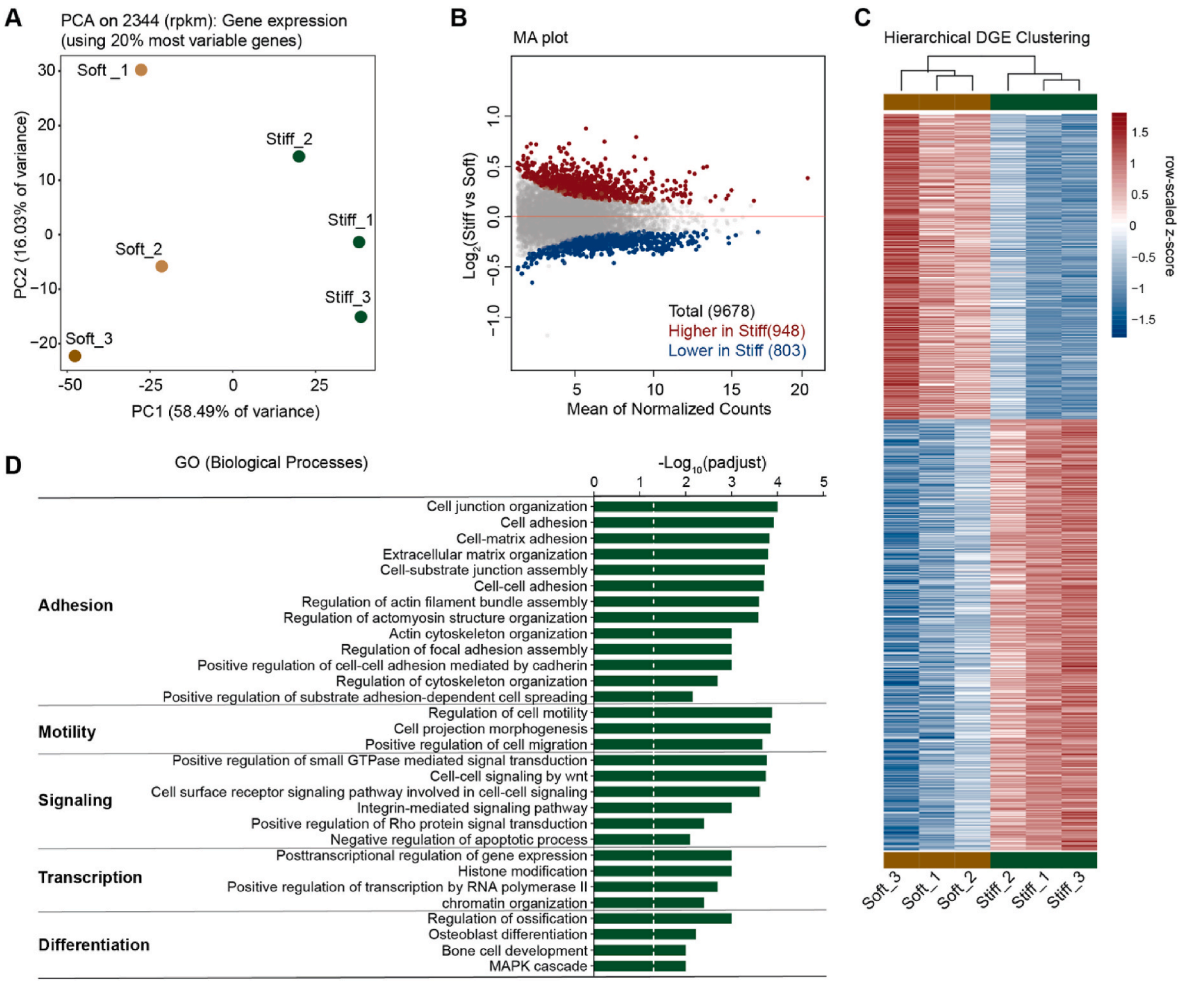

Fig. 2. Transcriptome perturbation in stiff nanoengineered hydrogels. **(A)** Principal component analysis (PCA) of replicate samples of hMSCs cultured within soft stiff hydrogels based on mRNA expression from RNAseq w.r.t. 20 % most variable genes across all replicates (n = 3). **(B)** Minus average (MA) representation of gene expression differences between stiff cultured-hMSCs and soft cultured-hMSCs where significant events are determined using GLM (*Padj.* < 0.05). Significantly highly expressed genes are depicted in red while genes with significantly low expression are depicted in blue. Events depicted in gray represent genes with non-significant differential expression. **(C)** Hierarchical clustering of replicate samples of hMSCs cultured within soft (tan) hydrogels and stiff (green) hydrogels. Differential gene expression (DGE, *Padj.* < 0.05) across all replicates are depicted as rows (n = 895) with highly expressed genes represented in red and genes with low expression represented in blue. Z-scoring represents row-scaled values. **(D)** Compiled gene ontology biological processes are arranged in categories for adhesion, motility, signaling, transcription, and differentiation. Significance values are reported as -Log10 transformation of *Padj.* < 0.05, threshold at x = 1.3 represented as white dotted line. (For interpretation of the references to color in this figure legend, the reader is referred to the Web version of this article.)

enrichment analysis were: Cell Junction Organization (GO:0034330), Cell Adhesion (GO:007155) and Cell-Matrix Adhesion (GO:0007160) (Fig. 3B). A range of important genes such as *VCAN*, *TLN1*, *LAMA4*, *ITGA11*, *EGFR*, *NTOCH1*, *PDLIM5* and *CLASP1* are upregulated on stiff hydrogels compared to soft hydrogels. These highly enriched GO terms indicate that high matrix stiffness affects the stability and organization of cell-cell and cell-matrix interactions.

Gene set enrichment analysis (GSEA) was used to further evaluate cell-ECM interactions. We looked for enrichment of *GO* and *Reactome* pathways in the pre-ranked list (by significance and fold-change direction) of all expressed genes. Positively enriched terms were grouped based on their similarity to cell surface adhesion and signaling events. The top results included: extracellular matrix organization, laminin interactions, cell matrix adhesion, cell-cell adhesion via plasma membrane adhesion molecules, and integrin cell surface interactions (Fig. 3C). These results suggest that matrix stiffness promotes ECM-cell interaction and is involved in cell spreading.

From DEGs, we identified that stiff hydrogels upregulated key integrins (*ITGA2/5/10/11)*, laminins (*LAMA2/3/4*, *LAMC1*, and *LAMB1)*, and collagens (*COL5A3, COL4A2, COL6A3*, and *COL4A1*), which facilitates matrix binding (Figs. S3B–E). This indicates that cells are proactive in remodeling their microenvironment by secreting nascent proteins. The presence of fibronectin (FN1) in stiff hydrogels, facilitates the binding of nascent proteins to the cell surface. Immunofluorescent staining of FN1 and entactin (NID1) at 72 h revealed localization at the periphery of hMSCs in stiff hydrogels, concomitant with the initiation of cellular spreading (Fig. 3D). Matrix remodeling were further investigated by assessing the compressive modulus of soft and stiff hydrogels embedded with hMSCs over a period of 7 days (Fig. 3E). A marked reduction in matrix stiffness was noted in stiff hydrogels, suggestive of active-matrix remodeling. Conversely, the modulus of soft hydrogels remained unchanged.

The remodeling of extracellular matrix and deposition of neo-ECM such as proteoglycans in stiff hydrogels is observed via upregulation of *VCAN*, heparin sulfate proteoglycan 2 (*HSPG2*), netrin 4 (*NTN4*), *ADAM19*, and matrix metallopeptidase 2 (*MMP2*) from RNA-seq data. To further validate the effect of stiffness on cell-induced remodeling, immunofluorescent staining was performed for intercellular adhesion molecule 1 (ICAM1). This adhesion molecule is expressed on the surface of cells and contributes to extracellular matrix organization. A

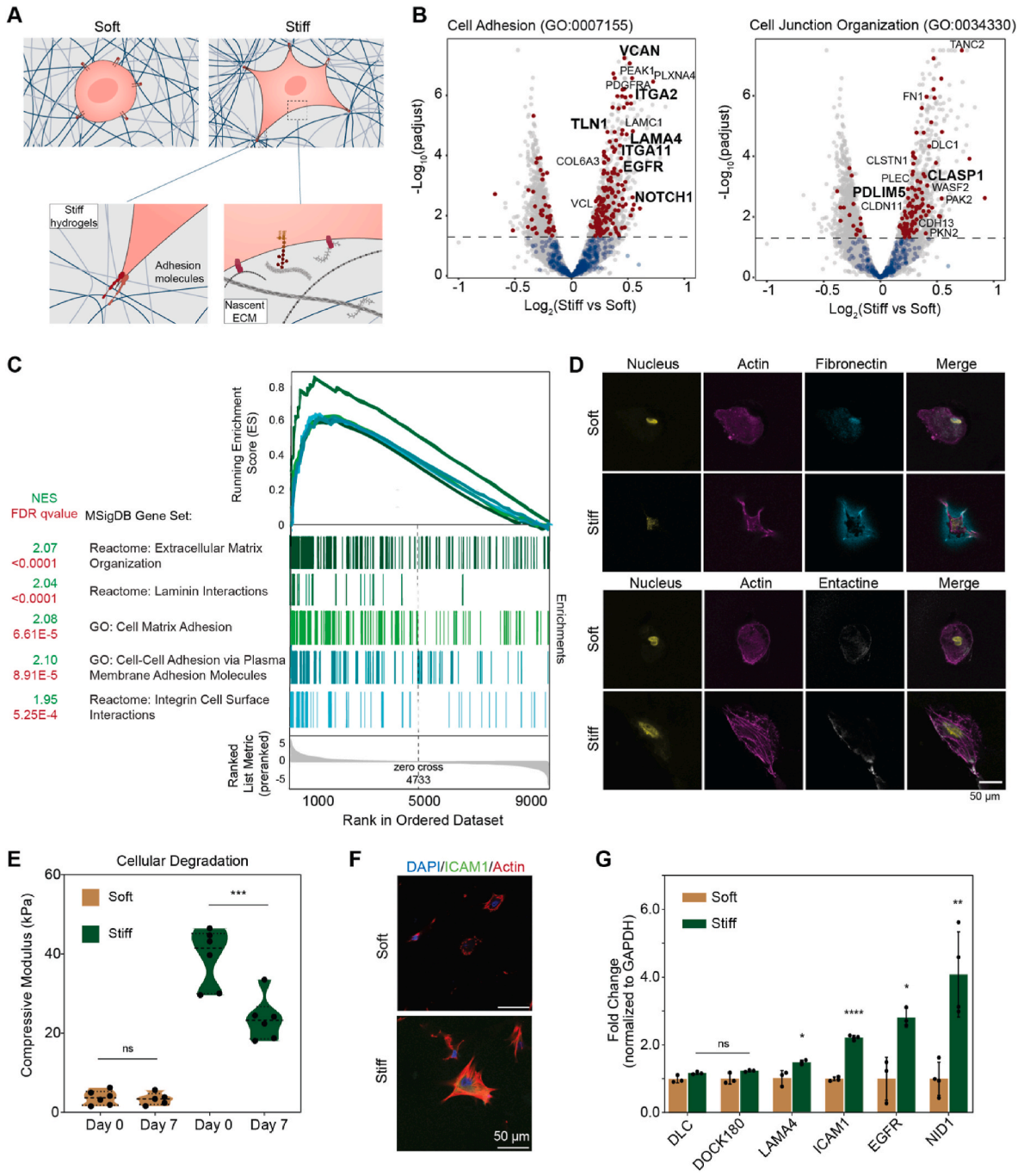

Fig. 3. Adhesion and surface-mediated signal activation by stiff nanoengineered hydrogels. **(A)** Schematic of relevant surface-mediated interactions between cells and matrix environment to initiate intracellular signaling. Interactions include orchestration of adhesion molecules (e.g., integrin clustering) and recruitment of nascent ECM proteins. **(B)** Volcano plot representation of significant DEGs (*Padj.* < 0.05) within Cell Adhesion (GO:0007155, left) and Cell Junction Organization (GO:0034330, right). Gray: all genes within background ontology. Blue: genes within the GO term that are below the significance threshold in our system. Red: Significant genes associated with the GO term. **(C)** Gene set enrichment analysis (GSEA) assessing matrix interactions including adhesion and ECM constituent coordination against curated *GO* and *Reactome* databases (*Padj.* < 0.05). **(D)** Immunofluorescent staining for fibronectin (FN1, cyan) and entactin (NID1, gray) illustrates organization of nascent protein at cell periphery in stiff hydrogels (bottom). Counterstained with F-actin (magenta) and DAPI (yellow). Scale bar 50 µm. **(E)** Compressive moduli of soft and stiff hydrogels after cell encapsulation for 7 days (n = 6, mean ± s.d., ns: nonsignificant, $^{**}P < 0.01$, unpaired two-tailed t tests). **(F)** Immunofluorescent staining for adhesion molecule 1 (ICAM1, green) reveals stiff hydrogels (right) promote higher ICAM1 expression in hMSCs than soft gels (left). Counterstained structures include F-actin (red) and DAPI (blue). Scale bar 50 µm. **(G)** Relative protein expression (normalized to soft samples) determined through enzyme linked immunosorbent assay (ELISA). Fold change quantification for each target corresponds to initial loading of total 20 µg protein per well normalized to GAPDH expression for each condition (n = 3, mean ± s.d., $^{****}P \leq 0.0001$, $^{**}P \leq 0.01$, $^{*}P \leq 0.05$, n.s. $P > 0.05$, unpaired two-tailed *t* tests). (For interpretation of the references to color in this figure legend, the reader is referred to the Web version of this article.)

significantly high expression of ICAM1 at the boundaries of projected actin structures was observed in cells encapsulated within stiff hydrogels compared to soft hydrogels (Fig. 3F, Fig. S5). To further support the differential expression of candidate DEGs at protein level, enzyme linked immunosorbent assay (ELISA) was also performed at Day 7. We confirmed the expression of ICAM1, DLC1, DOCK180, EGFR, LAMA4, and NID1, by ELISA in the soft and stiff conditions (Fig. 3G). A significant increase in the expression of LAMA4 (1.47-fold), ICAM1 (2.21-fold), EGFR (2.80-fold), and NID1 (4.08-fold) was observed. These data further support that stiff hydrogels facilitate ECM remodeling, and cell-matrix interactions by driving the expression of mechanically-sensitive genes.

2.5. Stiff matrices regulate focal adhesion complex formation

Evidence of increased cell elongation in stiff hydrogels led us to examine the regulation of intracellular cytoskeleton events. It is widely known that cells respond to the extracellular environment by altering actin filament dynamics [40]. Integrin mediate surface signaling, resulting in the formation of focal adhesion complexes [41], which grow through the recruitment of Rac [42], a member of the Rho GTPase family [43]. Tyrosine kinases are also phosphorylated, promoting growth and turnover of focal adhesion complexes [44]. Proteins like focal adhesion kinase (FAK) and paxillin are phosphorylated, creating binding sites for docking proteins, which drives complex growth [45]. Mechanosensitive proteins like talin 1 (TLN1) and vinculin (VCL) are activated by these interactions, linking polymerizing actin filaments to focal adhesion complexes, forming fibrillar adhesions [46]. As focal adhesions mature, the formation of stress fibers through another Rho-GTPase family effector, ROCK, allows external mechanical signals to be transmitted through actin filament contraction [47,48].

In this study, we investigated the expression of ROCK1, a downstream effector of the Rho signaling pathway, using immunostaining. We observed enhanced ROCK1 expression and cell spreading in stiff hydrogels, which is potentially due to the coordinated Rho signaling (Fig. 4A). This is supported by GO analysis which identified Actin Cytoskeleton Organization (GO:00300036) as one of the BP that is affected due to difference in matrix stiffness (Fig. 4B). Functionally, this translates to enhanced cell spreading, as demonstrated through a significant increase in F-actin expression in stiff hydrogels by immunostaining (Fig. 4C). Since past reports [49] and our own RNA-seq dataset implicates the role of TLN1 in growth of actin filaments, immunostaining was also performed against this target. As expected, enhanced localization of TLN1 was observed in stiff conditions, particularly at cell membrane boundaries (Fig. 4C, Figs. S5A–B). This demonstrates the recruitment of TLN1, a cytoskeletal protein in responding to mechanical forces. Quantification of TLN1 via ELISA confirmed significant increase (1.89-fold, $P < 0.0015$) in expression in stiff hydrogels (Fig. 4D). Additionally, ELISA and immunostaining of phosphorylated FAK (pFAK-Y397) showed increased pFAK expression in cells cultured in stiff

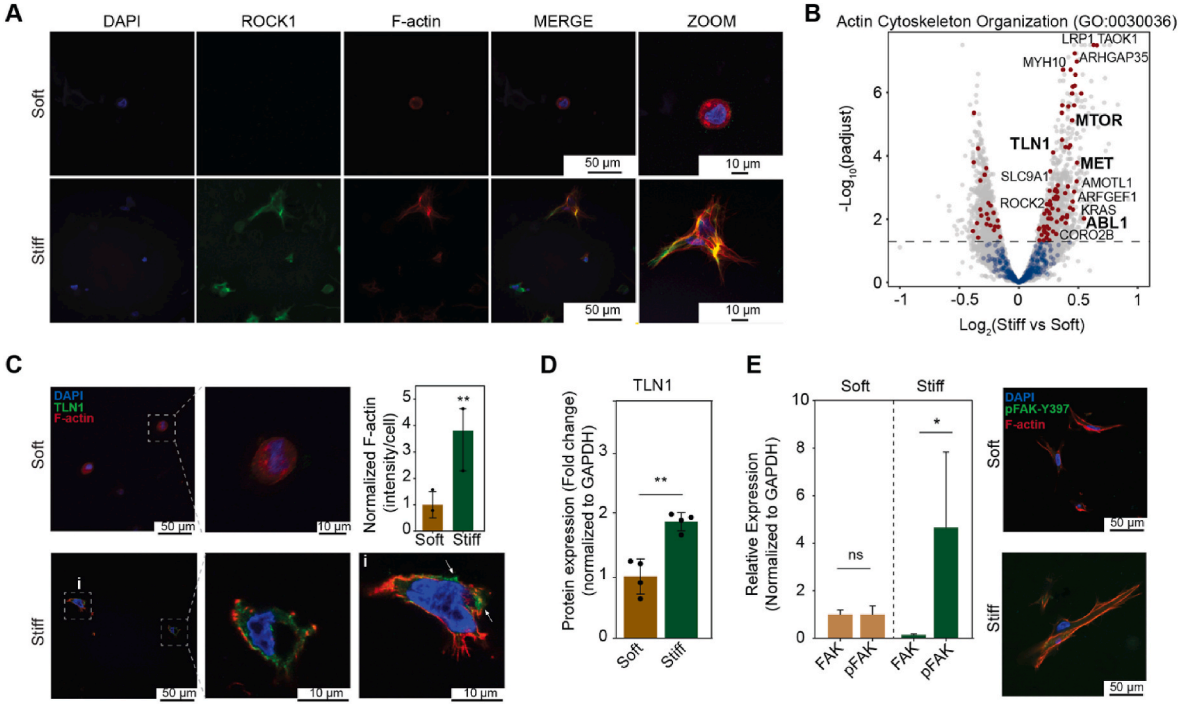

Fig. 4. Signal propagation in stiff nanoengineered hydrogels. **(A)** Immunofluorescent staining of Rho associated coiled-coil containing protein kinase 1 (ROCK1, green) expression in soft and stiff constructs after 5 days of encapsulation. Counterstaining of DAPI (blue) and F-actin filaments (red) illustrate nuclear and cytoskeletal cellular components. Scale bar, 100 μm; magnified scale bar, 50 μm. **(B)** Volcano plot representing significant DEGs (Padj. < 0.05) associated with Actin Cytoskeleton Organization (GO:0030036). Gray: all genes within background ontology. Blue: genes within the GO term that are below the significance threshold in our system. Red: Significant genes associated with the GO term. **(C)** Immunofluorescent staining of talin 1 (TLN1, green) expression in soft and stiff constructs after 7 days of encapsulation. Counterstaining of DAPI (blue) and F-actin filaments (red) illustrate the nuclear and cytoskeletal cellular components. White arrows depict regions of TLN1 aggregation which are present at sprouting points near the cell boundary. Quantification of F-actin performed via fluorescent intensity measurement (normalized to DAPI content) (**$P \leq 0.01$, unpaired two-tailed *t*-test). **(D)** Relative TLN1 protein expression (normalized to soft samples) determined through ELISA. Fold change quantification for each target corresponds to initial loading of total 20 μg protein per well normalized to GAPDH expression for each condition (n = 4, mean ± s.d., **$P \leq 0.01$, unpaired two-tailed *t* tests). **(E)** Relative focal adhesion kinase (FAK) and phosphorylated FAK (pFAK) expression (normalized to soft FAK level) determined through ELISA. Fold change quantification corresponds to initial loading of total 20 μg protein per well normalized to GAPDH expression for each condition (n = 3–4, mean ± s.e.m., ns: non-significant, *$P < 0.05$, unpaired two-tailed t tests). Immunofluorescent staining of phosphorylated focal adhesion kinase (pFAK, green) expression in soft (left) and stiff (right) constructs after 7 days of encapsulation. Counterstaining of DAPI (blue) and F-actin filaments (red). Representative images captured with 60x lens (scale bar, 50 μm). (For interpretation of the references to color in this figure legend, the reader is referred to the Web version of this article.)

hydrogels (Fig. 4E). While cells cultured within soft matrices do not show increase in FAK and pFAK, stiff hydrogels promote significantly higher pFAK expression (4.66-fold, $P < 0.0318$). These data collectively suggest that the differences at mRNA levels (by RNA-seq) of important mechanosensitive factors is also reflected at protein level. Similar results were shown earlier that pFAK expression presents as a diffuse cytoplasmic signal, rather than as distinct focal adhesion complexes in 3D culture [50].

From our GO analysis, we determined enrichment of Transmembrane Receptor Protein Tyrosine Kinase Signaling Pathway (GO:0007169) and Positive Regulation of GTPase Activity (GO:0043547) (Figs. S6A–B). To investigate the genes responsible for GTPase-mediated actin growth, DEGs that showed upregulation (*Padj.* < 0.05) and supported enrichment of cell projection morphogenesis (GO:0048858) and actin cytoskeleton organization (GO:0030036) were analyzed (Figs. S6C–D). GSEA analysis revealed significant positive enrichment of terms such as small GTPase-mediated signal transduction, Rho GTPase cycle, Rac 1 GTPase cycle, and signaling by receptor tyrosine kinases (Fig. S6E).

This is likely due to the coordination of genes including notch receptor 2 (*NOTCH2*), TAO kinase 1 (*TAOK1*), *TLN1*, and *VCL*. *NOTCH2* provides transmembrane receptor sites for transmitting signals from the extracellular environment to internal complexes, including notch intracellular domain (*NICD*). *TAOK1* stabilizes the cell cytoskeleton by facilitating tyrosine kinase receptor binding site phosphorylation. Both *TLN1* and *VCL* code for important mechanosensitive proteins that contribute to the maturation of focal adhesion complexes.

2.6. Enhanced cell-matrix adhesion trigger PI3K signaling

The analysis of DEGs in relation to Rho-mediated actin organization did not fully explain the maturation of focal adhesion complexes. To gain a better understanding of the signaling pathway involved in regulating focal adhesion formation and stress fiber assembly, GSEA was performed using the Wikipathways database. The top significantly enriched annotations included nine terms directly related to focal adhesion signaling pathways. To study the interaction between these terms, leading edge analysis was performed. This generated an enrichment map that visualized the similarities and highlighted the central members of each term (Fig. 5A). The analysis showed that focal adhesion assembly is closely related to the PI3AKT/mTOR signaling pathway, with three of the nine annotations describing focal adhesion, PI3AKT signaling, and focal adhesion PI3AKT mTOR signaling. These pathways are also connected to mRNA targets in the extracellular matrix, membrane receptors, Alpha 6 Beta 4 signaling pathway, and EGFR tyrosine kinase inhibitor receptors, which together form the five core members of the enrichment map.

Assessment of DEGs in the leading edges revealed that SOS Ras/Rac

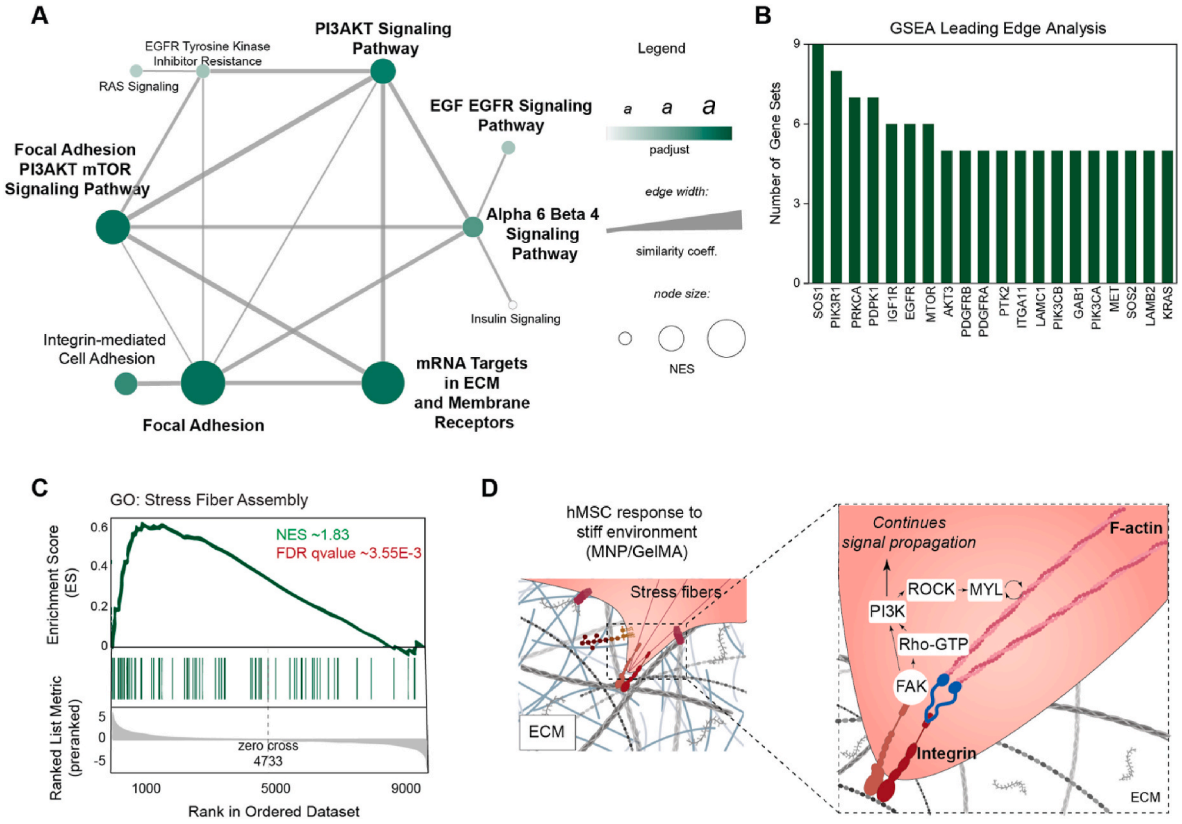

Fig. 5. Signal propagation in stiff nanoengineered hydrogels proceeds through PI3K pathway. **(A)** Signaling pathway is assessed by GSEA (*Padj.* < 0.1) against curated *Wikipathways* database and visualized through enrichment map network in Cytoscape. FDR-adjusted *P* values are represented gradiently as node fill color, while node size corresponds to normalized enrichment score (NES) of each category. Edge width represents Cytoscape-generated similarity coefficient (Jaccard) and illustrates how highly each category is connected to another in the network. **(B)** Leading edge DEGs were compiled for all nine terms built into the enrichment map to identify important DEGs in the signal propagation. Number of gene sets corresponds to how many terms in which a DEG contributes as a core enrichment (number of gene sets <5). **(C)** GSEA results illustrate positive enrichment of Stress Fiber Assembly (*GO* database) promoted by culture within nanoreinforced hydrogels (*Padj.* $<$ 0.01). Vertical green bars represent individual genes in the ranked list ordered by positive correlation (left) and negative correlation (right) to the term. Normalized enrichment scores (NES) correspond to the magnitude of correlation that genes in the ranked list have with the term normalized to term size. **(D)** Schematic of elucidated intracellular signaling mechanism. Initiated by surface interactions in response to increased matrix stiffness, PI3AKT signaling feeds F-actin polymerization and growth to allow cell motility and elongation. (For interpretation of the references to color in this figure legend, the reader is referred to the Web version of this article.)

guanine nucleotide exchange factor 1 (SOS1) is a member of all nine terms (Fig. 5B, Fig. S7A). The role of SOS1 in the regulation of focal adhesion and stress fiber assembly is supported by its involvement in PI metabolism [51], which is a necessary process in the production of other signaling molecules in the PI3AKT cascade (Fig. S7B). Pathway visualization analysis showed that PIK3R1 is central to both processes, stimulating DEGs such as epidermal growth factor receptor (*EGFR)*, protein tyrosine phosphatase nonreceptor type 11 *(PTPN11)*, and *SOS1* in the cell projection morphogenesis group, and KRAS proto-oncogene, GTPase (*KRAS),* platelet derived growth factor receptor alpha *(PDGFRA),* 3 phosphoinositide dependent kinase 1 (*PDPK1)*, and lysophosphatidic acid receptor 1 (*LPAR1)* in the actin cytoskeleton organization group (Fig. S8A). The overlap between focal adhesion formation and stress fiber assembly was analyzed by examining related GO terms and actomyosin structure regulation (Fig. S8B). The results from GSEA showed a positive correlation with stress fiber assembly (GO:0043149) against the MSigDB c5 Ontology database (Fig. 5C, Fig. S9A-L). The regulation of the key gene *PIK3R1* was modeled to compare its regulation in soft and stiff matrices (Fig. S8C). It is evident that the maturation of pFAK assemblies in stiff hydrogels is driven by the activation of the PI3AKT-mTOR signaling transduction (Fig. 5D).

The involvement of the PI3K/mTOR pathway in mechanotransduction has been well-documented, particularly within the realm of cancer mechanobiology [52,53]. PI3K activation is a known response to mechanical cues such as substrate stiffening [54], matrix contraction [55], and integrin-induced tension [56]. Upon integrin aggregation at the cell-extracellular matrix (ECM) junction, the formation of active FAK complexes and the recruitment of vinculin, talin, and actin filaments facilitate the accumulation of PIP3. This messenger (PIP3) is instrumental in activating downstream effectors like AKT, which then initiate a cascade of phosphorylation events [57,58]. These events culminate in the modulation of gene expression through epigenetic mechanisms. For instance, hyperactive PI3K signaling in cancer cells leads to dysregulated transcription, promoting cell proliferation and survival [59,60]. Similar cascades are implicated in the osteogenic response to mechanical stimuli; for example, the PI3K inhibitor LY294002 has been shown to dampen osteoblast differentiation on modified implant surfaces [61]. The regulation of hMSC osteogenesis involves the interplay between cell surface caveolae, adhesion receptors, and subsequent PI3K/AKT signaling [62]

2.7. Matrix stiffness remodels YAP1-accessible chromatin landscape

Recent studies have reported role of biophysical characteristics to influence epigenetic landscape in stem cells [6,63,64]. These have largely been explored in 2D cell culture models to understand the effect of substrate stiffness and microtopographic patterns [4,65]. Our GO analysis also showed that histone modification (GO:0016570) and chromatin organization (GO:0006325) BPs were significantly affected by matrix stiffness (Fig. 6A–B, S10). One alteration that can occur in response to changes in the extracellular environment is the acetylation of lysine 27 of histone 3 (H3K27ac) [66,67]. This modification is facilitated by histone acetyltransferases (HATs) and is associated with active chromatin. H3K27ac mark has been shown at active promoters and enhancers [66]. Another important modification is DNA methylation, typically associated with the repression of gene transcription if present at gene promoters and transcription elongation if present within gene bodies [68,69]. Early stages of cell reprogramming involve removal of these groups via demethylases [70]. Additionally, histone methylation plays varying roles in activation and inhibition of transcription. Methylation at particular histone lysine (K) residues (e.g. K4, K36, K79) have been generally established as activation marks [71–73].

To explore terms related to histone modifications, positively correlated GSEA terms were examined. Six terms were identified, including Chromatin Modifying Enzymes, Histone Lysine N-Methyltransferase Activity, O-Linked Glycosylation, PKMTs Methylate Histone Lysines, HATS Acetylate Histones, and HDMS Demethylate Histones (Fig. S11A). Analysis of leading-edge genes within these GO terms revealed that the genes responsible for coding HATs were upregulated in hMSCs cultured in stiff hydrogels. Specifically, CREB binding protein (*CREBBP*) and E1A binding protein p300 (*EP300*) were found to be upregulated (Fig. 6A–C, S11B). These co-activators assist in the nuclear localization of Yes-associated protein 1 (YAP1) and serve as HATS [51,74]. The nuclear localization of Yes-associated protein 1 (YAP1) is a crucial marker of the canonical YAP/TAZ mechanotransduction pathways, which convert mechanical signals into biological effects [75].

Several methylases and demethylases are differentially regulated in hMSCs cultured in stiff matrices, including Tet methylcytosine dioxygenase 2 (*TET2*), lysine methyltransferase 2A (*KMT2A*), lysine demethylase 2A (*KDM2A*), and histone lysine methyltransferase complex subunit (*ASH2L*) (Fig. 6C). In oncogenic environments, it has been proposed that both DNA and histone methylation modifiers, such as TET2 and KDM2A, are transcribed following YAP1/TEAD binding [76].

We validated these RNA-seq observations via qRT-PCR that confirms differentiation regulation of *EP300, KDM2A* and *TET2* in stiff matrix (Fig. 6D).

To confirm the anticipated localization of YAP1, immunostaining was performed after 3 days of culture on stiff nanoreinforced hydrogels, which showed that, YAP1 underwent nuclear translocation in the stiff constructs while soft hydrogels maintained YAP1 in the cytoplasm (Fig. 6E). The ratio of YAP1 nuclear versus cytoplasmic content was determined through subcellular fractionation and ELISA protein assessment. The results showed a greater than 3-fold increase in the YAP1 nuclear:cytoplasmic ratio in stiff hydrogels compared to soft gels, confirming the movement of YAP1 into the nucleus and its activation as a transcription factor co-activator (Fig. 6F). Further, digestion of nuclear extracts with micrococcal nuclease to recover chromatin-bound proteins revealed a significant increase in chromatin-bound YAP1. The coverage plot of *YAP1* further illustrates that nanoreinforced stiff hydrogels enhance the expression of this gene (Fig. S12A). RNA-seq data were validated via qRT-PCR analysis. Compared to soft controls, stiff hydrogels were found to upregulate *YAP1* in hMSCs after 7 days of culture (Fig. S12B).

We employed ChIP-qPCR assay focusing to quantify H3K27ac levels for established YAP1-regulated genes (**Methods**). Cells encapsulated in stiff hydrogels were significantly enriched for H3K27ac, as compared to soft hydrogels, highlighting the correlation between mechanical stiffness and epigenetic modulation. We found enrichment of DNA fragments associated with H3K27ac for connective tissue growth factor (*CTGF*, 1.76-fold, $P < 0.0013$) and kisspeptin 1 (*KISS1*, 2.05-fold, $P < 0.0027$) (Fig. 6G) in stiff hydrogels compared to soft ones. Regulation of these genes is supported by RNA-seq analysis (Table S1). This coordinated process appears essential for the regulation of genes related to osteogenic lineage.

3. Conclusion

Engineered biomaterials are a valuable tool for studying mechanotransduction and the impact of biophysical factors on cellular behavior. However, traditional 2D microenvironments do not fully replicate the complex 3D microenvironments found *in vivo*, which can result in different cell-ECM interactions and mechanisms of mechanotransduction. However, the interplay between 3D confinement, ECM properties, and cell behavior remains poorly understood, especially the role of matrix stiffness. To address this gap, we have leveraged a nanoengineered approach to reinforce polymeric hydrogels and investigate the impact of stiffness on cellular behavior without altering other biophysical factors. The crosslinking mechanism resulted in a ten-fold increase in stiffness, and hMSCs on stiff hydrogels displayed an elongated morphology while those on soft hydrogels were circular. The stiff hydrogels initiated a surface-mediated transmission of mechanical signals that propagated through Rho GTPase-activated PI3AKT signaling

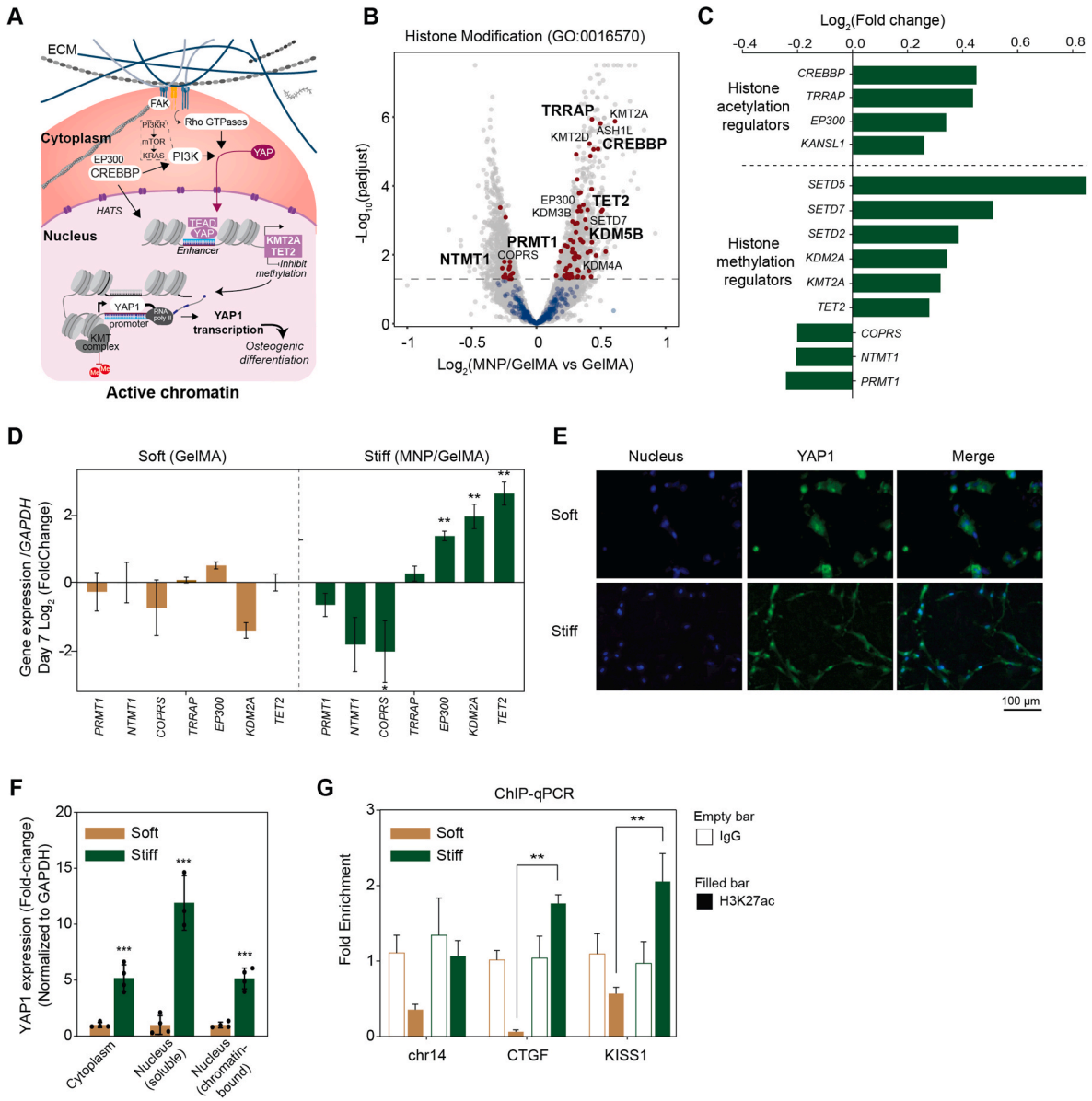

Fig. 6. Histone remodeling in stiff nanoengineered hydrogels to allow YAP1 binding. **(A)** Schematics representing interplay of mechanical signal transduction and epigenetic remodelers in driving YAP1 nuclear localization, binding at TEAD1 promoter region, and transcription of osteogenic factors. **(B)** Volcano plot representing significant DEGs (*Padj.* < 0.05) within Histone Modification (GO:0016570). Gray: all genes within background ontology. Blue: genes within the GO term that are below the significance threshold in our system. Red: Significant genes associated with the GO term. **(C)** Leading edge DEGs contributing to positive enrichment of GSEA terms HATS Acetylate Histones and HDMS Demethylate Histones illustrated (*Padj.* < 0.05). Log_2 transformed fold changes are represented nominally on the x-axis. **(D)** Gene expression of key epigenetic regulators identified through RNA-seq analysis are validated using qRT-PCR after 7 days of culture within soft and stiff hydrogels. Log_2 transformed fold changes are represented versus each gene target, normalized to soft samples (n = 4, mean ± s.d., unpaired two-tailed *t*-test). **(E)** Immunofluorescent staining of YAP1 (green) is localized to the nucleus in hMSCs cultured on stiff hydrogels (bottom) after 3 days compared to indiscriminate localization (cytoplasm and nucleus) in soft hydrogels (top). Blue represents DAPI nuclear counterstain. Scale bar, 100 μm. **(F)** Subcellular fractionation of YAP1 extracted from soft and stiff hydrogels after 7 days. Relative YAP1 protein expression (normalized to soft samples) determined through ELISA. Fold change quantification corresponds to initial loading of total 20 μg protein per well (n = 3, $^{***}P < 0.001$) normalized to GAPDH expression for each condition. Bars represent fold change normalized to soft hydrogels (n = 3, mean ± s.d., $^{*}P \leq 0.05$, unpaired two-tailed *t*-test). YAP1 localization ratio calculated as YAP1 expression in cytoplasmic fraction divided by nuclear fraction. **(G)** Quantification of H3K27ac associated DNA fragments for regulatory regions of *CTGF*, *KISS1*, and *chr14* (housekeeping) from hMSCs cultured in soft and stiff hydrogels for 7 days by ChIP-qPCR. Data are represented as fold enrichment of targets in anti-H3K27ac (filled) samples compared to anti-IgG (non-filled) samples for each condition (n = 4, mean ± s.e.m., $^{**}P < 0.005$, two-way ANOVA). (For interpretation of the references to color in this figure legend, the reader is referred to the Web version of this article.)

cascades, ultimately driving histone remodeling and binding to enhancer regions to sustain differentiation through a positive feedback loop. Our study sheds light on using engineered matrices to direct cell differentiation by highlighting the significance of matrix stiffness as an important biophysical factor. Unlike previous studies that used glycation approaches to modulate gel stiffness [77], which modified integrin binding sites and inhibited matrix degradability, the use of ultralow concentrations of nanoparticles did not impact chemical composition, ligand density, or degradability of hydrogel network. Overll, nanoengineered biomaterials in this study has implications for the development of biomimetic materials to model cell behavior in native 3D environments for regenerative medicine and cancer bioengineering.

Funding

A.K.G. acknowledges financial support from the National Institute of Biomedical Imaging and Bioengineering (NIBIB) of NIH, the Director's New Innovator award (DP2 EB026265), Peer Reviewed Medical Research Program (PRMRP) of Department of Defense (DOD) (W81XWH2210932), President's Excellence Fund (X-Grants) from Texas A&M University. I.S acknowledge financial support from National Institute of Neurological Disorders and Stroke (NINDS) (R21 NS121945) and Cancer Prevention and Research Institute of Texas (CPRIT) grant # RP230204. T.P.L. acknowledges financial support from the CPRIT-established investigator award grant # RR200043. The content is solely the responsibility of the authors and does not necessarily represent the official views of the funding agencies.

4. Materials and methods

4.1. Materials

Ferric chloride hexahydrate ($FeCl_3.6H_2O$, ≥98 %), Oleic acid (≥99 %), sodium oleate (≥99 %), polyethylene glycol (PEG, mol. wt. 600), ammonium persulphate (APS, 98 %), sodium metabisulfite (SBS, 99 %), crosslinker *N,N′*-methylene-bis-acrylamide (MBAAm), Doxorubicin.HCl (DOX, HPLC grade), DCC (*N,N′*-dicyclohexylcarbodiimide), *N*-hydroxysuccinimide (NHS), dopamine hydrochloride (dopamine 98 %) and solvents hexane, ethanol, dimethyl sulfoxide (DMSO), dichloromethane (DCM) and chloroform were all purchased from Sigma Aldrich, USA. All chemicals were directly used without further purification.

4.2. Hydrogel synthesis

Iron oxide polyethylene glycol (PEG)-dopamine-nanoparticles were synthesized according to previously published methods to yield 8 nm particles[31]. Briefly, nanocrystals were formed via bottom-up synthesis from ferric chloride hexahydrate and sodium oleate. The iron oleate complex then underwent decomposition at increasing temperature, wherein the reaction was heated to 70 °C for 4 h. The mixture was then washed with ultrapure water until solvent dissipation. The yield was dissolved in 1-octadecane and oleic acid, then slowly heated to a final temperature of 315 °C until formation of 8 nm oleic acid-functionalized nanocrystals, approximately 10 min.

To produce aqueous stable nanoparticle suspensions, hydrophobic particles were functionalized with PEG diacid. Briefly, anchoring ligand nitro-dopamine supplied dual hydroxyl groups to oxidize and bind to iron groups on the nanoparticle surface, thus facilitating the replacement of aliphatic chains with stabilizing PEG via 1-ethyl-3-(3-dimethyl aminopropyl) carbodiimide (EDC) – N-hydroxysuccinimdie (NHS) chemistry. Moreover, adding nitro groups stabilized the particles through creation of electron deficiency, aiding oxidation by hydroxyl groups. The entire reaction was performed while stirring and sonicating for approximately 48 h.

For hydrogel synthesis, gelatin methacrylol (GelMA) precursor solution in deionized water were prepared with and without nanoparticles, constituting control (5 % (w/v) GelMA) and nanoreinforced hydrogels (5 μg/mL nanoparticles in 5 % (w/v) GelMA) groups. Precursor solutions were subsequently crosslinked under ultraviolet (UV) light (OmniCure Series 2000) at an intensity of 30 mW/cm^2 for 60 s. Intensity of UV light was validated using a radiometer prior to crosslinking of each sample group. Crosslinking was performed on coverslips with PDMS molds to yield gels with uniform dimensions of 4 mm diameter by 0.5 mm thickness. Crosslinked gels were suspended in PBS and stored at room temperature until characterization.

4.3. Mechanical and rheological characterization

Stiffness of crosslinked gels was determined through uniaxial measurement of Young's modulus on a mechanical tester (Xpert 7600, ADMET). Gels underwent uniaxial compression at a continuous strain rate of 1 mm/min. Then, compressive modulus was calculated from the linear region of the stress-strain curve (force divided by original cross-sectional area). Rheological characteristics were evaluated using a stress-controlled rheometer (DHR-2 Discovery hybrid, TA Instruments) with a 8 mm parallel plate geometry at 0.8 mm gap with solvent trap attachment. All rheological experiments were performed on solid cylindrical hydrogel samples of 4 mm × 0.5 mm (diameter x thickness) dimensions. Stress sweep was conducted under constant oscillatory strain to determine storage (G') and loss (G'') moduli. Stress relaxation was performed with incrementally increasing magnitudes of applied strain (5, 10, 15, and 20 %). To evaluate rate of stress relaxation, constant 15 % strain was applied to hydrogel samples and moduli values were normalized to initial values for each sample. Normalized stress relaxation half-life ($\tau_{1/2}$) was taken to be the time at which the modulus decreased to half of the initial value.

4.4. Enzymatic degradation

Crosslinked hydrogels (soft and stiff) were washed once in PBS and transferred to solutions of 0.15 and 1.5 U/mL collagenase type 2. Gels were incubated for 5 days at 37 °C. Degradation was quantified via mass measurement normalized to day 0.

4.5. 3D cell encapsulation within hydrogels

2D-seeded hMSCs (passage <5) were collected via trypsinization and pelleted via centrifugation at 1000 rpm for 5 min. Cell density was determined via counting on an EVE Automatic Cell Counter (NanoEnTek) with Trypan blue to determine live cell number. Cells were resuspended in basal media (αMEM supplemented with 16.5 % FBS and 1 % P/S) and incorporated into gel precursor solutions to yield a final density of 50,000 cells/mL. Gels were crosslinked upon coverslips as previously described and incubated in basal media at 37 °C with 5 % CO_2 for 7 days, with media being replaced every 2 days.

4.6. Differentiation of hMSCs

Cells were encapsulated as previously described and cultured in either osteogenic (αMEM supplemented with 10 mM β-glycerophosphate and 50 μM ascorbic acid) or adipogenic (DMEM supplemented with 0.5 μM dexamethasone, 0.5 μM isobutylmethylxanthine, and 50 μM indomethacin) media for 21 days. Whole gels were fixed in 4 % paraformaldehyde and stained with Alizarin Red S (pH 4.2) or Oil Red O for approximately 30 min. Excess stain was rinsed 3 times with PBS. Stained gels were imaged with Zeiss SteREO brightfield microscope. Quantification of calcium deposits and lipid nodules was performed via overnight stain dissolution in cetylpyridinium chloride (CPC) or IPA, respectively, and spectrophotometric absorbance measurement at 405 nm and 525 nm using Cytation 5 (Biotek).

4.7. Transcriptome sequencing (RNA-seq)

After 7 days, gels were permeabilized with 0.1 % Triton X-100 in PBS followed by extraction of mRNA using the Zymogen Quick RNA Miniprep kit. To assess mRNA quality prior to sequencing, quantification of nucleic acid content was determined using NanoDrop® and an absorbance ratio threshold of $A_{260}/A_{280} > 2$ was set to standardize mRNA quality. Sequencing was performed on the BGI DNA Nanoball (DNB™) platform to yield 20–30 million reads per sample of 75 paired ends.

Following sequencing, reads were trimmed and aligned in reference to the human genome (hg38, GRCh37 Genome Reference Consortium Human Reference 37, obtained from University of California, Santa Cruz) using the R-Bioconductor package Spliced Transcripts Aligned to a Reference (STAR). mRNA levels of stiff sample group were compared to

soft sample group to determine stiffness-induced differential gene expression (DEG). For negative control soft sample group (hMSCs cultured within hydrogels composed of 5 % GelMA), 34,346,529 (32,221,196 uniquely mapped), 34,201,844 (32,149,421 uniquely mapped), and 34,062,051 (31,957,714 uniquely mapped) reads were aligned to the genome for the three replicates. For the stiff sample group, 34,288,470 (32,195,930 uniquely mapped), 33,836,793 (31,788,650 uniquely mapped), and 34,170,317 (31,993,211 uniquely mapped) reads were aligned to the genome for the three replicates. In further analysis, only uniquely mapped reads were used. RefSeq gene models were retrieved from UCSC and expression was quantified to read counts using the uniquely mapped reads of the coding exons, normalized by gene length using reads per kilobase of transcript per million mapped reads (RPKM) factor. Minimal to no expression genes were removed with RPKM less than 1. Genes with RPKM greater than 1 in at least half (0.5) of replicates for each condition were considered expressed. Bioconductor package DESeq2 was used to model genes expressed in distinct conditions (i.e., differentially expressed genes) via negative binomial distribution. High dimensional clustering (HDC) was then performed using Log2-adjusted RPKM. DEGs were sorted with a statistical threshold (Benjaminin-Hochberg false discovery rate (FDR) adjust), *Padj.* < 0.05.

Statistically significant DEGs were used to calculate functional annotation enrichment of gene ontology (GO) terms belonging to Biological Processes (BP), Cellular Components (CC), and Molecular Functions (MF) ontologies using Bioconductor package GoStats conditional hyperGTest of overrepresentation. Gene set enrichment analysis (GSEA) was performed using the GSEA java desktop application against the current Molecular Signatures Database (v7.4 MSigDB). DEGs rank lists were constructed according to the following function: Rank = -Log_{10}(Pvalue)*sign (FoldChange). Ranked lists were uploaded to the GSEA desktop application and used in performing GSEAPreranked analysis where test parameters were default against the Chip platform "Human_ENSEMBL_Gene_ID_MSigDB.v7.5.chip". Probed databases included current releases of curated Hallmarks (h.all.v7.5.symbols.gmt), Reactome (c2.cp.reactome.v7.5.symbols.gmt), Wikipathways (c2.cp.wikipathways.v7.5.symbols.gmt), and GO (c5.all.v7.5.symbols.gmt). Enriched GSEA terms are represented using Log10 transformation of FDR-adjusted *P* value (i.e., Q value) and normalized enrichment score (NES). DEGs comprising the leading edge of an enriched term (i.e., core enrichments) were selected for further analysis. Organization and network visualization of enriched GO and GSEA terms was performed using available online software including Cytoscape.

4.8. Live/dead staining of 3D-encapsulated hMSCs

hMSCs were encapsulated at predefined density (10 [5] cells/mL) in the appropriate precursor solution (GelMA or nanoreinforced GelMA hydrogels) and subsequently crosslinked using UV light (30 mW/cm^2 for 60s) as previously described. After 1, 3, and 5 days of cell encapsulation, the normal media was removed and the hydrogels were washed with PBS. Prepared Live/Dead assay reagent (Calcein AM and Ethidium Homodimer; Santa Cruz Biotechnology, Inc., USA) were added to the specimen and incubated at 37 °C for 30 min. Samples were then washed 2X with PBS and imaged using a Zeiss Axio Observer Z1 microscope. ImageJ plugin *Analyze Particles* was used to measure area and circularity of captured cells.

4.9. Immunofluorescent staining of 3D-encapsulated hMSCs

To visualize cell cytoskeleton, F-actin filaments were immunostained using Acti-stain™ 670 phalloidin (Cytoskeleton, Inc.) according to the manufacturer's protocol. Briefly, hMSCs were encapsulated for 7 days in hydrogels (n = 4). After 7 days, gels were washed in PBS and fixed in 4 % paraformaldehyde (PFA) for 10 min at room temperature. Gels were permeabilized in 0.5 % TritonX-100 for 5 min at room temperature and washed with PBS. Gels were blocked using SuperBlock T-20 (Thermo Scientific) for 1 h at room temperature. Gels were stained with 200 nM Acti-stain™ for 45 min at 37 °C, protected from light, then washed thrice with 1x PBST. DAPI counterstain (0.5 μg/mL) was performed for 15 min at 37 °C. For immunofluorescent detection of other targets, rabbit polyclonal primary antibodies sourced from ProteinTech with IgG isotype were diluted in blocking buffer and incubated overnight at 4 °C, then washed thrice. Gels were incubated in goat anti-rabbit IgG secondary antibody (AF488, 1:1000) diluted in blocking buffer for 1–2 h at room temperature, protected from light, then washed thrice. All washing was performed using 1x PBST for 5 min per change at room temperature. Stained hMSCs were imaged using a Zeiss LSM 780 Multiphoton confocal microscope. All images were taken at a random z-position of 4 replicates for each lens (20x, 60x), processed in ImageJ, and one representative image presented.

4.10. qRT-PCR

Quantitative real-time polymerase chain reaction (qRT-PCR) was performed on the QuantStudio™ 3 System (Applied Biosystems). Comparative C_T ($\Delta\Delta C_T$) experiments were designed with endogenous control GAPDH. Total 40 cycles passed through Hold (2 min 50 °C, 10 min 95 °C), PCR (15 s 95 °C, 1 min 60 °C), and Melt Curve (15 s 95 °C, 1 min 60 °C, 15 s 95 °C) stages. Total volume per well was 20 μL. mRNA was extracted at 3, 5, and 7 days after encapsulation with soft and stiff gels using previously described extraction method. mRNA was stored at −80 °C until use. To prepare cDNA, mRNA was mixed with nuclease-free water to final concentration of 100 ng in a reaction tube per 15 μL, then 5 μL qScript 5X cDNA Supermix (QuantaBio) was added. Contents were vortexed and centrifuged for few seconds to ensure complete mixing. Then, cDNA precursors were cycled according to manufacturer's directions on a thermocycler (EdvoCycler). Briefly, incubate at 25 °C for 5 min, 42 °C for 30 min, and 85 °C for 5 min cDNA was stored at 4 °C until use within 2 days. For PCR amplification, cDNA was diluted 10x and 2 μL volume was added to each well of a 96-well Optical Clear MicroAmp™ EnduraPlate™ (Applied Biosystems). Primers for genes of interest were designed using Primer-BLAST to generate forward and reverse (5′ to 3′) sequences and manufactured by ThermoFisher Custom Oligo. The following forward/reverse (F/R) primers were used for gene validation:

GAPDH: F – GTCTCCTCTGACTTCAACAGCG, R – ACCACCCTGTTGCTGTAGCCAA.

YAP1: F – GATCCCGGGCAGCAGCCG, R – GCTATAACCATGTAAGAAAGC.

EP300: F – AGCAGCGGCCGTATTTATTTATTTTC, R – CCAGCCGAGGTCTCTCGGA.

CREBBP: F – GCCAGCACCACCTACAATCGT, R – AAGAAACCTGGAAAGCCCCAAC.

COPRS: F – CAGGGACTTTAAATGAAGTAGTGAAGG, R –AAAATGTTTGCAGTGACCCCTAGT.

KMT2A: F – CCCGAGGCCGCTATACAGATT, R – CCTGAAGAGGCTGAGGACGATGA.

KDM2A: F – CCGAGCCCTGGAAGAACGC, R – CCCAGTCGCAGAAGAGGGATT.

NTMT1: F – CAGCATGTTCCCAGGTTTCAGGT, R – GGCTTCAGCACAGAATCCCACTG.

PRMT1: F – CATCCCGGGTCGACTTGAGG, R – GGGATAAGACCCTCCGCTAGG.

TET2: F – CGGAATTAGCTCTGTATCGGTCGG, R – TGCACTCCACCACCACTTCG.

TRRAP: F – GGGATTTAAAGGGCCGGGACC, R – GTCCCAGGCCGAGCTACG.

Master mixes of gene targets were produced from F/R primers (0.6 μL/well, 10 μM), SYBR® Green (10.8 μL/well), and nuclease-free water. Total 18 μL volume of master mix was added to each well containing sample cDNA. The plate was sealed and centrifuged for 30 s at 1000 rpm

to concentrate contents.

4.11. Chromatin immunoprecipitation and gene expression

Isolation of chromatin complexes was achieved using a modified Cleavage Under Targets & Release Using Nuclease (CUT&RUN) protocol [78,79]. Briefly, cells were fixed in 0.1 % formaldehyde for 2 min followed by quenching with glycine for 5 min. Pelleted cells were washed, mixed with concanavalin A-coated beads, and bound cells isolated on a magnet stand. Primary antibody (H3K27ac, IgG) incubation occurred overnight, then isolation of antibody-bound complexes was performed via Protein A/G-MNase binding and calcium digestion. DNA was purified using Qiagen Gel Purification kit. Primers for downstream targets of *YAP1* and housekeeping control *chr14* with the following F/R sequences were used for ChIP-qPCR:

Chr14: F – GTGGGCCTTTGGAATATCCT, R – GACCTTGGCTGTGTTGTCCT, chr14:66,894,932–66,895,059.

CTGF: F – GCCAATGAGCTGAATGGAGT, R – CAATCCGGTGTGAGTTGATG, chr10:92,681,001–92,681,083.

KISS1: F – CTTTCCATCCTCCACACCCT, R – ACTAGGTGTGTCTGTGGCTC, chr1:204,164,957-204,165,098.

Analysis of the presence of DNA fragments was performed using fold enrichment method according to established protocols.

4.12. Protein quantification

Protein was extracted from hMSCs encapsulated within hydrogels after 7 days of 3D culture via RIPA buffer lysis. Hydrogels were washed once with cold PBS, then homogenized in 500 μL RIPA Lysis and Extraction Buffer (ThermoFisher Scientific) supplemented with 0.5 μL Halt Protease Inhibitor Cocktail to avoid protein degradation. Samples were incubated on ice in RIPA solution for 30 min, then centrifuged to pellet debris. Supernatant containing protein was stored at −20 °C until further use. MicroBCA™ Protein Assay Kit was used to quantify protein concentration of extracted samples according to manufacturer's protocol. Indirect ELISA was performed in Nunc MaxiSorp™ flat-bottom plates where 20 μg/mL total protein was loaded per well and allowed to attach during overnight incubation at 4 °C. After washing, primary antibodies were diluted according to manufacturer recommendation for ELISA detection. Primary antibodies included polyclonal rabbit anti-ICAM1 (1:1000), anti-LAMA4 (1:500), anti-NID1 (1:1000), anti-DOCK180 (1:1000), anti-EGFR (1:1000), anti- TLN1 (1:500), anti-DLC1 (1:200), anti-ROCK1 (1:500), anti-FAK (1:500), and anti-YAP (1:500). Each polyclonal primary antibody was sourced from ProteinTech with IgG isotype.

Following primary antibody overnight incubation at 4 °C, H&L-conjugated goat anti-rabbit polyclonal secondary antibody was applied to each well and incubated at room temperature for 2 h. SuperSignal Plus West Femto solution was then applied for detection. Fluorescence intensity sweep was performed immediately after adding detection solution (fixed 355 nm Ex, sweep 400–500 nm Em by 10 nm, gain 75). Each sample was corrected by blank (no antigen) reads and normalized to soft sample average to obtain relative protein expression.

4.13. Subcellular protein fractionation

Protein was extracted from hMSCs cultured for 7 days in soft and stiff hydrogels and separated for each subcellular compartment using Subcellular Protein Fractionation Kit for Cultured Cells (ThermoFisher Scientific) according to manufacturer's directions. Briefly, gels were dissociated via manual homogenization with pestle and cells were harvested via centrifugation at 500×*g* for 5 min. Stepwise extraction buffers were added according to manufacturer's instructions followed by centrifugation to isolate compartmentalized protein contents. All extraction buffers contained Halt™ Protease Inhibitors to mitigate degradation during extraction. All steps were performed at 4 °C with ice-cold reagent solutions unless otherwise specified in kit instructions. Protein fractions were stored at −80 °C until use. Fractions were processed for protein quantification via ELISA.

4.14. Statistical analysis

All statistical analysis was performed using GraphPad Prism. One-way analysis of variance (ANOVA) coupled with Tukey's post hoc were performed. Unpaired two-tailed *t* tests were used to perform statistical analysis between the stiff hydrogel and soft hydrogel samples for IF, PCR, and ELISA. Plots were graphed as means and standard deviation (s.d.), and statistical significance is presented as *P ≤ 0.05; **P ≤ 0.01; ***P ≤ 0.001, ****P ≤ 0.0001. All images are representative of compiled samples from 3 to 4 independent experiments.

Credit Author Statement

Anna L. Kersey: Conceptualization, Experimental Design, Methodology, Investigation, Visualization, Writing – Original Draft Preparation; Led the study's conceptualization and was responsible for experimental design. Key in methodology development and investigation, as well as in visualizing data. Took the lead in writing the original draft of the manuscript.Daniel Y. Cheng: Methodology; Contributed specifically to the methodology, focusing on data collection using quantitative polymerase chain reaction (qPCR).Kaivalya A. Deo: Methodology; Involved in the methodology, specifically in rheology.Christina R. Dubell: Methodology; Assisted in methodology, especially in confocal imaging.Ting-Ching Wang: Methodology; Contributed to the methodology, particularly in confocal imaging.Manish K. Jaiswal: Methodology; Involved in methodology, focusing on the synthesis and modification of magnetic nanoparticles and rheology.Min Hee Kim: Methodology; Contributed to the methodology, particularly in the synthesis and modification of magnetic nanoparticles.Aparna Murali: Methodology; Contributed to the methodology, specifically in ChIP-PCR.Sarah Hargett: Methodology; Contributed to the methodology, specifically in the area of rheology. Sumana Mallick: Methodology; Involved in the methodology, focusing on ChIP-PCR.Tanmay P. Lele: Methodology; Involved in Funding Acquisition, and methodology, specifically in confocal imaging.Akhilesh K. Gaharwar: Conceptualization, Supervision, Funding Acquisition, Investigation, Visualization, Writing – Original Draft Preparation, Writing – Review & Editing; Contributed significantly to the conceptualization, supervision, and funding acquisition for the study. Actively involved in the investigation and visualization of data. Played a central role in both drafting and revising the manuscript.Irtisha Singh: Conceptualization, Supervision, Funding Acquisition, Investigation, Visualization, Writing – Original Draft Preparation, Writing – Review & Editing; Significantly contributed to the study's conceptualization and supervision. Instrumental in funding acquisition, participating in the investigation, and data visualization. Engaged in the initial drafting and revising of the manuscript.All Coauthors: Writing – Review & Editing; All coauthors participated in commenting on the results and in critically revising the manuscript.

Declaration of competing interest

The authors declare that they have no known competing financial interests or personal relationships that could have appeared to influence the work reported in this paper.

Data availability

All data needed to evaluate the conclusions in the paper are present in the paper and/or the Supplementary Materials. Raw data used to generate figures is available through Figshare data repository.

Acknowledgments

We acknowledge the contribution of Dr. Karli Gold for RNA-seq sample preparation. Portions of this research were conducted with the advanced computing resources provided by Texas A&M High Performance Research Computing. Confocal microscopy was performed in part with equipment at Texas A&M College of Medicine Integrated Microscopy and Imaging Laboratory (RRID:SCR_021637). All the figures were organized in Adobe Illustrator.

Appendix ASupplementary data

Supplementary data to this article can be found online at https://doi.org/10.1016/j.biomaterials.2024.122473.

References

[1] A. Saraswathibhatla, D. Indana, O. Chaudhuri, Cell–extracellular matrix mechanotransduction in 3D, Nat. Rev. Mol. Cell Biol. 24 (2023) 495–516.
[2] C. Bonnans, J. Chou, Z. Werb, Remodelling the extracellular matrix in development and disease, Nat. Rev. Mol. Cell Biol. 15 (2014) 786–801.
[3] C. Loebel, R.L. Mauck, J.A. Burdick, Local nascent protein deposition and remodelling guide mesenchymal stromal cell mechanosensing and fate in three-dimensional hydrogels, Nat. Mater. 18 (2019) 883–891.
[4] S. Nemec, K.A. Kilian, Materials control of the epigenetics underlying cell plasticity, Nat. Rev. Mater. 6 (2021) 69–83.
[5] S. Dupont, S.A. Wickström, Mechanical regulation of chromatin and transcription, Nat. Rev. Genet. 23 (2022) 624–643.
[6] T.L. Downing, et al., Biophysical regulation of epigenetic state and cell reprogramming, Nat. Mater. 12 (2013) 1154–1162.
[7] A. Gaharwar, I. Singh, A. Khademhosseini, Engineered biomaterials for in situ tissue regeneration, Nat. Rev. Mater. 5 (2020) 686–705.
[8] K.H. Vining, D.J. Mooney, Mechanical forces direct stem cell behaviour in development and regeneration, Nat. Rev. Mol. Cell Biol. 18 (2017) 728–742.
[9] D.E. Discher, P. Janmey, Y.-l. Wang, Tissue cells feel and respond to the stiffness of their substrate, Science 310 (2005) 1139–1143.
[10] A.J. Engler, S. Sen, H.L. Sweeney, D.E. Discher, Matrix elasticity directs stem cell lineage specification, Cell 126 (2006) 677–689.
[11] A.S. Mao, J.-W. Shin, D.J. Mooney, Effects of substrate stiffness and cell-cell contact on mesenchymal stem cell differentiation, Biomaterials 98 (2016) 184–191.
[12] J.H. Wen, et al., Interplay of matrix stiffness and protein tethering in stem cell differentiation, Nat. Mater. 13 (2014) 979.
[13] N. Huebsch, et al., Harnessing traction-mediated manipulation of the cell/matrix interface to control stem-cell fate, Nat. Mater. 9 (2010) 518–526.
[14] C. Yang, et al., Spatially patterned matrix elasticity directs stem cell fate, Proc. Natl. Acad. Sci. USA 113 (2016) E4439–E4445.
[15] K.M. Yamada, M. Sixt, Mechanisms of 3D cell migration, Nat. Rev. Mol. Cell Biol. 20 (2019) 738–752.
[16] D.L. Bodor, W. Pönisch, R.G. Endres, E.K. Paluch, Of cell shapes and motion: the physical basis of animal cell migration, Dev. Cell 52 (2020) 550–562.
[17] O. Chaudhuri, et al., Hydrogels with tunable stress relaxation regulate stem cell fate and activity, Nat. Mater. 15 (2016) 326–334.
[18] M.P. Lutolf, J.A. Hubbell, Synthetic biomaterials as instructive extracellular microenvironments for morphogenesis in tissue engineering, Nat. Biotechnol. 23 (2005) 47–55.
[19] F. Grinnell, C.-H. Ho, E. Tamariz, D.J. Lee, G. Skuta, Dendritic fibroblasts in three-dimensional collagen matrices, Mol. Biol. Cell 14 (2003) 384–395.
[20] W.P. Daley, K.M. Gulfo, S.J. Sequeira, M. Larsen, Identification of a mechanochemical checkpoint and negative feedback loop regulating branching morphogenesis, Dev. Biol. 336 (2009) 169–182.
[21] V.Z. Beachley, et al., Tissue matrix arrays for high-throughput screening and systems analysis of cell function, Nat. Methods 12 (2015) 1197–1204.
[22] K. Adebowale, et al., Enhanced substrate stress relaxation promotes filopodia-mediated cell migration, Nat. Mater. 20 (2021) 1290–1299.
[23] T. Luo, et al., A review on the design of hydrogels with different stiffness and their effects on tissue repair, Front. Bioeng. Biotechnol. 10 (2022) 817391.
[24] C. Dannert, et al., Nanoparticle-hydrogel composites: from molecular interactions to macroscopic behavior, Polymers 11 (2) (2019) 275.
[25] S.R. Shin, B. Aghaei-Ghareh-Bolagh, T.T. Dang, S.N. Topkaya, X. Gao, S.Y. Yang, S. M. Jung, J.H. Oh, M.R. Dokmeci, X. Tang, et al., Cell-laden microengineered and mechanically tunable hybrid hydrogels of gelatin and graphene oxide, Adv. Mater. 25 (2013) 6385–6391.
[26] S.R. Shin, H. Bae, J.M. Cha, J.Y. Mun, Y.-C. Chen, H. Tekin, H. Shin, S. Farshchi, M. R. Dokmeci, S. Tang, et al., Carbon nanotube reinforced hybrid microgels as scaffold materials for cell encapsulation, ACS Nano 6 (2012) 362–372.
[27] S.R. Shin, S.M. Jung, M. Zalabany, K. Kim, P. Zorlutuna, S.b. Kim, M. Nikkhah, M. Khabiry, M. Azize, Kong, et al., Carbon-nanotube-embedded hydrogel sheets for engineering cardiac constructs and bioactuators, ACS Nano 7 (2013) 2369–2380.
[28] J.R. Xavier, T. Thakur, P. Desai, M.K. Jaiswal, N. Sears, E. Cosgriff-Hernandez, R. Kaunas, A.K. Gaharwar, Bioactive nanoengineered hydrogels for bone tissue engineering: a growth-factor-free approach, ACS Nano 9 (2015) 3109–3118. D. Chimene, C. Peak, J. Gentry, J. Carrow, L. Cross, E. Mondragon, G. Cardoso, R. Kaunas, A. Gaharwar, Nanoengineered Ionic-Covalent Entanglement (NICE) Bioinks for 3D Bioprinting, ACS Applied Materials & Interfaces 10(12) (2018) 9957–9968; L.M. Cross, J.K. Carrow, X. Ding, K.A. Singh, A.K. Gaharwar, Sustained and Prolonged Delivery of Protein Therapeutics from Two-Dimensional Nanosilicates, ACS Applied Materials & Interfaces 11(7) (2019) 6741–6750.
[29] N.A. Jalili, M.K. Jaiswal, C.W. Peak, L.M. Cross, A.K. Gaharwar, Injectable nanoengineered stimuli-responsive hydrogels for on-demand and localized therapeutic delivery, Nanoscale 9 (2017) 15379–15389.
[30] K.A. Deo, M.K. Jaiswal, S. Abasi, G. Lokhande, S. Bhunia, T.-U. Nguyen, M. Namkoong, K. Darvesh, A. Guiseppi-Elie, L. Tian, Nanoengineered ink for designing 3D printable flexible bioelectronics, ACS Nano 16 (6) (2022) 8798–8811. M.K. Jaiswal, J.K. Carrow, J.L. Gentry, J. Gupta, N. Altangerel, M. Scully, A.K. Gaharwar, Vacancy-Driven Gelation Using Defect-Rich Nanoassemblies of 2D Transition Metal Dichalcogenides and Polymeric Binder for Biomedical Applications, Advanced Materials 29(36) (2017) 1702037. H.P. Lee, G. Lokhande, K.A. Singh, M.K. Jaiswal, S. Rajput, A.K. Gaharwar, Light-Triggered In Situ Gelation of Hydrogels using 2D Molybdenum Disulfide (MoS2) Nanoassemblies as Crosslink Epicenter, Advanced Materials 33(23) (2021) 2101238.
[31] M.K. Jaiswal, et al., Mechanically stiff nanocomposite hydrogels at ultralow nanoparticle content, ACS Nano 10 (2016) 246–256.
[32] D. Indana, P. Agarwal, N. Bhutani, O. Chaudhuri, Viscoelasticity and adhesion signaling in biomaterials control human pluripotent stem cell morphogenesis in 3D culture, Adv. Mater. 33 (2021) 2101966.
[33] J. Park, et al., Control of stem cell fate and function by engineering physical microenvironments, Integr. Biol. 4 (2012) 1008–1018.
[34] S.B. Han, J.K. Kim, G. Lee, D.H. Kim, Mechanical properties of materials for stem cell differentiation, Advanced Biosystems 4 (2020) 2000247.
[35] C. Yang, M.W. Tibbitt, L. Basta, K.S. Anseth, Mechanical memory and dosing influence stem cell fate, Nat. Mater. 13 (2014) 645–652.
[36] F. Guilak, et al., Control of stem cell fate by physical interactions with the extracellular matrix, Cell Stem Cell 5 (2009) 17–26.
[37] A. Dobin, et al., STAR: ultrafast universal RNA-seq aligner, Bioinformatics 29 (2013) 15–21.
[38] S. Anders, W. Huber, Differential expression analysis for sequence count data, Genome Biol. 11 (2010) R106.
[39] G.S. Hussey, J.L. Dziki, S.F. Badylak, Extracellular matrix-based materials for regenerative medicine, Nat. Rev. Mater. 3 (2018) 159–173.
[40] S. Walcott, S.X. Sun, A mechanical model of actin stress fiber formation and substrate elasticity sensing in adherent cells, Proc. Natl. Acad. Sci. USA 107 (2010) 7757–7762.
[41] M.R. Chastney, J.R. Conway, J. Ivaska, Integrin adhesion complexes, Curr. Biol. 31 (2021) R536–R542.
[42] J.T. Parsons, K.H. Martin, J.K. Slack, J.M. Taylor, S.A. Weed, Focal Adhesion Kinase: a regulator of focal adhesion dynamics and cell movement, Oncogene 19 (2000) 5606–5613.
[43] J. Tcherkezian, N. Lamarche-Vane, Current knowledge of the large RhoGAP family of proteins, Biol. Cell. 99 (2007) 67–86.
[44] S.K. Mitra, D.A. Hanson, D.D. Schlaepfer, Focal adhesion kinase: in command and control of cell motility, Nat. Rev. Mol. Cell Biol. 6 (2005) 56–68.
[45] D.J. Webb, et al., FAK–Src signalling through paxillin, ERK and MLCK regulates adhesion disassembly, Nat. Cell Biol. 6 (2004) 154–161.
[46] J.T. Parsons, A.R. Horwitz, M.A. Schwartz, Cell adhesion: integrating cytoskeletal dynamics and cellular tension, Nat. Rev. Mol. Cell Biol. 11 (2010) 633–643.
[47] T. Leung, X.-Q. Chen, E. Manser, L. Lim, The p160 RhoA-binding kinase ROK alpha is a member of a kinase family and is involved in the reorganization of the cytoskeleton, Mol. Cell Biol. 16 (1996) 5313–5327.
[48] S. Tojkander, G. Gateva, P. Lappalainen, Actin stress fibers – assembly, dynamics and biological roles, J. Cell Sci. 125 (2012) 1855–1864.
[49] A. Del Rio, et al., Stretching single talin rod molecules activates vinculin binding, Science 323 (2009) 638–641. Nardone, G. et al. YAP regulates cell mechanics by controlling focal adhesion assembly. Nature Communications 8, 15321 (2017).
[50] S.I. Fraley, et al., A distinctive role for focal adhesion proteins in three-dimensional cell motility, Nat. Cell Biol. 12 (2010) 598–604. Cukierman E. et al., Taking Cell-Matrix Adhesions to the Third Dimension, Science (80) 294 (2001) 1708-1713.
[51] M. Delvecchio, J. Gaucher, C. Aguilar-Gurrieri, E. Ortega, D. Panne, Structure of the p300 catalytic core and implications for chromatin targeting and HAT regulation, Nat. Struct. Mol. Biol. 20 (2013) 1040–1046.
[52] B. Vanhaesebroeck, et al., The emerging mechanisms of isoform-specific PI3K signalling, Nat. Rev. Mol. Cell Biol. 11 (5) (2010) 329–341.
[53] A.N. Gargalionis, et al., mTOR signaling components in tumor mechanobiology, Int. J. Mol. Sci. 23 (3) (2022) 1825.
[54] A. Husain, et al., Substrate stiffening promotes VEGF-A functions via the PI3K/Akt/mTOR pathway, Biochem. Biophys. Res. Commun. 586 (2022) 27–33.
[55] H. Xia, et al., Focal adhesion kinase is upstream of phosphatidylinositol 3-kinase/Akt in regulating fibroblast survival in response to contraction of type I collagen matrices via a β1 integrin viability signaling pathway, J. Biol. Chem. 279 (31) (2004) 33024–33034.
[56] R.W. Tilghman, J.T. Parsons, Focal adhesion kinase as a regulator of cell tension in the progression of cancer. Seminars in Cancer Biology, Elsevier, 2008.
[57] A. Toker, C.C. Dibble, PI 3-kinase signaling: AKTing up inside the cell, Mol. Cell 71 (6) (2018) 875–876.
[58] B.D. Manning, A. Toker, AKT/PKB signaling: navigating the network, Cell 169 (3) (2017) 381–405.

[59] Y. He, et al., Targeting PI3K/Akt signal transduction for cancer therapy, Signal Transduct. Targeted Ther. 6 (1) (2021) 425.
[60] A. Saraswathibhatla, et al., Cell–extracellular matrix mechanotransduction in 3D, Nat. Rev. Mol. Cell Biol. 24 (7) (2023) 495–516.
[61] Z. Zheng, et al., Involvement of PI3K/AKT signaling pathway in promoting osteogenesis on titanium implant surfaces modified with novel non-thermal atmospheric plasma, Front. Bioeng. Biotechnol. 10 (2022) 975840.
[62] N. Baker, et al., Promotion of human mesenchymal stem cell osteogenesis by PI3-kinase/Akt signaling, and the influence of caveolin-1/cholesterol homeostasis, Stem Cell Res. Ther. 6 (1) (2015) 238.
[63] Y. Li, et al., Biophysical regulation of histone acetylation in mesenchymal stem cells, Biophys. J. 100 (2011) 1902–1909.
[64] A.R. Killaars, et al., Extended exposure to stiff microenvironments leads to persistent chromatin remodeling in human mesenchymal stem cells, Adv. Sci. 6 (2019) 1801483.
[65] L. Larsson, S.P. Pilipchuk, W.V. Giannobile, R.M. Castilho, When epigenetics meets bioengineering—a material characteristics and surface topography perspective, J. Biomed. Mater. Res. B Appl. Biomater. 106 (2018) 2065–2071.
[66] S.M. Gorisch, M. Wachsmuth, K.F. Tóth, P. Lichter, K. Rippe, Histone acetylation increases chromatin accessibility, J. Cell Sci. 118 (2005) 5825–5834.
[67] R. Marmorstein, S.Y. Roth, Histone acetyltransferases: function, structure, and catalysis, Curr. Opin. Genet. Dev. 11 (2001) 155–161.
[68] S.U. Kass, D. Pruss, A.P. Wolffe, How does DNA methylation repress transcription? Trends Genet. 13 (1997) 444–449.
[69] H. Cedar, Y. Bergman, Linking DNA methylation and histone modification: patterns and paradigms, Nat. Rev. Genet. 10 (2009) 295–304.
[70] S.K. Bhattacharya, S. Ramchandani, N. Cervoni, M. Szyf, A mammalian protein with specific demethylase activity for mCpG DNA, Nature 397 (1999) 579–583.
[71] J.C. Eissenberg, A. Shilatifard, Histone H3 lysine 4 (H3K4) methylation in development and differentiation, Dev. Biol. 339 (2010) 240–249.
[72] K. Hyun, J. Jeon, K. Park, J. Writing Kim, Erasing and reading histone lysine methylations, Exp. Mol. Med. 49 (2017) e324-e324.
[73] R.A. Varier, H.T.M. Timmers, Histone lysine methylation and demethylation pathways in cancer, Biochim. Biophys. Acta Rev. Canc 1815 (2011) 75–89.
[74] C. Das, et al., Binding of the histone chaperone ASF1 to the CBP bromodomain promotes histone acetylation, Proc. Natl. Acad. Sci. USA 111 (2014) E1072–E1081.
[75] G. Halder, S. Dupont, S. Piccolo, Transduction of mechanical and cytoskeletal cues by YAP and TAZ, Nat. Rev. Mol. Cell Biol. 13 (2012) 591–600.
[76] M. Jang, et al., Matrix stiffness epigenetically regulates the oncogenic activation of the Yes-associated protein in gastric cancer, Nat. Biomed. Eng. 5 (2021) 114–123.
[77] B.N. Mason, A. Starchenko, R.M. Williams, L.J. Bonassar, C.A. Reinhart-King, Tuning three-dimensional collagen matrix stiffness independently of collagen concentration modulates endothelial cell behavior, Acta Biomater. 9 (2013) 4635–4644.
[78] P.M. Michael, et al., A streamlined protocol and analysis pipeline for CUT&RUN chromatin profiling, bioRxiv (2019) 569129.
[79] P.J. Skene, S. Henikoff, An efficient targeted nuclease strategy for high-resolution mapping of DNA binding sites, Elife 6 (2017) e21856.